

Tomography of flavoured leptogenesis with primordial blue gravitational waves

Marco Chianese,^{1,2, a} Satyabrata Datta,^{3, b} Rome Samanta,^{4,2, c} and Ninetta Saviano^{2, 4, d}

¹*Dipartimento di Fisica "Ettore Pancini", Università degli studi di Napoli*

"Federico II", Complesso Universitario Monte S. Angelo, I-80126 Napoli, Italy

²*INFN - Sezione di Napoli, Complesso Universitario Monte S. Angelo, I-80126 Napoli, Italy*

³*Department of Physics and Institute of Theoretical Physics,*

Nanjing Normal University, Nanjing, 210023, China

⁴*Scuola Superiore Meridionale, Università degli studi di Napoli*

"Federico II", Largo San Marcellino 10, 80138 Napoli, Italy

We explore a scenario where an early epoch of matter domination is driven by the mass scale M_N of the right-handed neutrinos, which also characterizes the different flavour regimes of leptogenesis. Such a matter-domination epoch gives rise to peculiar spectral imprints on primordial Gravitational Waves (GWs) produced during inflation. We point out that the characteristic spectral features are detectable in multiple frequency bands with current and future GW experiments in case of Blue GWs (BGWs) described by a power-law with a positive spectral index ($n_T > 0$) and an amplitude compatible with Cosmic Microwave Background (CMB) measurements at the CMB scale. We find that the three-flavour leptogenesis regime with $M_N \lesssim 10^9$ GeV imprints BGWs more prominently than the two-flavour and one-flavour regimes characterized by a higher right-handed neutrino mass scale. In particular, a two-flavour (three-flavour) leptogenesis regime is expected to leave distinct imprints in the mHz-Hz (μHz -mHz) band. Moreover, we translate the current Big Bang Nucleosynthesis (BBN) and LIGO limits on the GW energy density into constraints on the flavour leptogenesis parameter space for different GW spectral indices n_T . We provide a rigorous statistical analysis of how the future GW detectors would be conjointly able to distinguish the flavour regimes. Interestingly, the scenario also offers unique GW signals testable in the next LIGO run with a correlated signature in the PTA frequency band with an amplitude comparable to the one expected from supermassive black holes.

CONTENTS

I. Introduction	2
II. Scalar field dynamics and the scale of thermal leptogenesis	4
III. Imprints of flavour regimes of leptogenesis on BGWs	10
IV. Results	13
V. Summary	18
Acknowledgements	19
A. Varying the $B - L$ gauge coupling	19
References	19

^a marco.chianese@unina.it

^b amisatyabrata703@gmail.com

^c samanta@na.infn.it

^d nsaviano@na.infn.it

I. INTRODUCTION

Primordial Gravitational Waves (GWs) can be a unique probe of physics operating at super high-energy scales that are otherwise unreachable, e.g., with terrestrial accelerators. Broadly, a high-energy theory/model can be sensitive to GWs in two ways. First, the model can accommodate a source of GWs whose amplitude and spectral features relate to the model parameters. Thus, the model becomes testable with the GW searches. On the other hand, the model can leave its imprints on GWs, regardless of how they are produced. This article discusses the latter case. Let us assume a spectrum of primordial GWs, which might be of inflationary origin [1, 2], and we aim at probing a post-inflation high-energy model with those GWs. In a given scenario where the underlying dynamics of GWs production are known, we expect specific spectral features in the GWs today. Therefore, testing an independent model (which is not related to the origin of GWs) would require finding detectable imprints in those GWs caused exclusively by the model under consideration. This method proposed as a tomographic search of BSM theories with GWs [3, 4] is similar to X-ray tomography of an object, wherein the object is placed in front of an X-ray source, and we let the X-ray pass through the object to know the invisible internal properties of the object. Likewise, the GW tomography has two main ingredients: the source, specifically the GW spectrum, and the object, namely the high-energy model to be tested.

In this article, for GW spectrum, we consider primordial Blue Gravitational Waves (BGWs) with $\Omega_{\text{GW}} \sim f^{n_T}$ (here Ω_{GW} is the GWs energy density, f is the frequency and $n_T > 0$ is a spectral index)¹ which might come, e.g., from inflation. For the high-energy model we want to probe, we consider thermal leptogenesis, which is a process that generates the baryon asymmetry of the universe [5]. BGWs are appealing by several considerations. First, for $n_T > 0$, the BGWs come with strong amplitude, and therefore, they are easily detectable, given the projected sensitivities of the current and planned GW detectors operating at different frequency bands. Second, the recent finding of nHz stochastic GWs by the Pulsar Timing Arrays (PTAs) shows a strong preference for a blue-tilted GW spectrum of primordial origin [6–17]. Specifically, a power-law fit to the 15 yrs NANOGrav PTA data renders a large spectral index value; $n_T \sim 1.2 - 2.4$ at 68% CL [10]. Third, because of their potentially strong amplitude in the sub-nHz and μHz regions, primordial BGWs are among the very few candidates that can be tested with pulsar parameter drifts [18, 19] and possibly with Lunar Laser Ranging (LLR) [20, 21]. Finally, as recently pointed out, BGWs might affect large-scale structures by sourcing density perturbations at second order [22]. Although we shall not provide any model that might produce such BGWs, let us mention that the simplest single-field slow-roll inflation models produce a nearly scale-invariant spectrum with very small amplitude. Nonetheless, plenty of scenarios [23–32] go beyond the simplest one and predict BGWs that are detectable at future GW experiments [33–45].

Leptogenesis [5] is a two-step process: a lepton asymmetry is created in the first step, which is then processed to a baryon asymmetry via the sphaleron transition [46]. Among several possibilities to generate lepton asymmetry [47–49], here we consider the one within the seesaw framework of light neutrino masses. In this scenario, CP-violating and out-of-equilibrium decays of right-handed (RH) neutrinos to lepton and Higgs doublet produce lepton asymmetry. Typically, at a temperature $T \sim M_N$, where M_N is the RH neutrino mass scale, lepton asymmetry gets produced. Depending on the several variants, a wide range of RH neutrino mass window, $M_N \in [\text{MeV}, 10^{15}\text{GeV}]$ [50–59], might facilitate a successful leptogenesis. As it is obvious, $M_N \gtrsim \mathcal{O}(\text{TeV})$ scales are not reachable with collider experiments, leptogenesis operating on those scales requires alternative probes. A way to test such a high-scale scenario is provided by the flavour effects [60–62] which connect it indirectly to low-energy neutrino observables, specifically to the leptonic CP violation

¹ As we discuss later, in a realistic setting it should be a broken power-law; otherwise the spectrum would not be cosmologically viable.

[63]. A flavoured leptogenesis scenario can have three distinct regimes (as described in the next section): one-flavour/vanilla regime (1FL) for $M_N \gtrsim 10^{12}$ GeV, two-flavour regime (2FL) for 10^{12} GeV $\gtrsim M_N \gtrsim 10^9$ GeV, and three-flavour regime (3FL) for $M_N \lesssim 10^9$ GeV. Though connecting those regimes with low-energy neutrino observables is possible, it is difficult to differentiate them observationally because of plenty of free parameters in seesaw models. One way to distinguish them is to impose further symmetries in the Lagrangian, e.g., discrete symmetries, to reduce the number of parameters [64, 65]. Here, we shall show that, alternatively, with the GW-tomography method, not only can such high scales be probed, but different flavour regimes can potentially leave distinct imprints on the BGW spectrum.

As outlined, given an independent source of GWs, testing a model requires finding imprints on the GW spectrum caused by the model. Therefore, probing different mass scales of leptogenesis (hence different flavour regimes) requires finding characteristic GW spectral features dependent on RH masses. We show that, though nontrivial, this can be done within some parameter space in the seesaw models, which offers an RH neutrino mass-dependent matter epoch affecting the standard propagation (in radiation domination) of primordial BGWs. The idea is based on contemplating the origin of RH neutrino masses. Let us suppose that, like any other Standard Model (SM) particles, the RH neutrinos get their mass via a phase transition triggered by an SM singlet scalar field. Once the field rolls down to its vacuum and attains its vacuum expectation value, besides generating RH neutrino masses, it oscillates coherently around the vacuum. Such oscillations persist long with a null equation of state parameter (the field behaves like matter) when the scalar field lives longer. Suppose the coupling of the scalar field to the RH neutrino plays a pivotal role in determining its lifetime. In that case, the duration of the matter domination can be controlled by the coupling and, therefore, by the RH neutrino masses. This is the key aspect of our study. Irrespective of their origin, as primordial gravitational waves pass through such a matter-dominated phase, the beginning and the end of the matter-dominated phase get imprinted on the final GW spectrum. Therefore, the final GW spectrum carries imprints of the RH neutrino mass scale. A probable timeline in the scenario has been illustrated in Fig. 1.

Within a concrete model of $U(1)_{B-L}$ phase transition² triggered by a scalar field Φ carrying $B-L$ charge, the key feature of our study is that a peaked BGW spectrum gets distorted when it passes through such an RH neutrino mass-dependent matter epoch and finally exhibits a double-peaked spectrum. The locations of the low-frequency peak ($f_{\text{low}}^{\text{peak}}$) and the dip (f^{dip}) in between are strongly sensitive to RH neutrino masses. As the leptogenesis process enters from an unflavoured to flavour regimes, these two characteristic frequencies shift from a high to a low-frequency value. For a three-flavour regime, we can obtain the ratio $\Omega_{\text{GW}}(f_{\text{low}}^{\text{peak}})/\Omega_{\text{GW}}(f^{\text{dip}})$ (the spectral distortion) much higher than the other flavour regimes. While the vanilla leptogenesis scenario hardly imprints the GW spectrum, the two-flavour and the three-flavour regimes exhibit characteristic spectral features in the GWs mostly in the mHz-Hz and μHz -mHz bands. The scenario can accommodate a reasonably large value of n_T without contradicting any cosmological constraints and allows the overall spectrum to span a wide range of frequencies accessible to the current and planned GW detectors. Notably, in the PTA frequency band, flavoured leptogenesis regimes allow GW amplitude comparable to supermassive black hole binaries (SMBHB) with a correlated high-frequency signal testable in the next LIGO run.

The rest of the paper is organized as follows. In Sec. II, we discuss the scalar field dynamics and all the constraints the model must comply with. In Sec. III, we describe the spectral distortions induced by the model on GW signals. In Sec. IV, we present a detailed numerical study on how the BGW spectrum contains information on the RH neutrino mass scale and recast the current BBN and LIGO limits into bounds of the model parameter space. We also discuss our model in the

² In the seesaw Lagrangian, $U(1)_{B-L}$ may naturally arise as a residual symmetry of many Grand Unification Theories (GUT) [66–70].

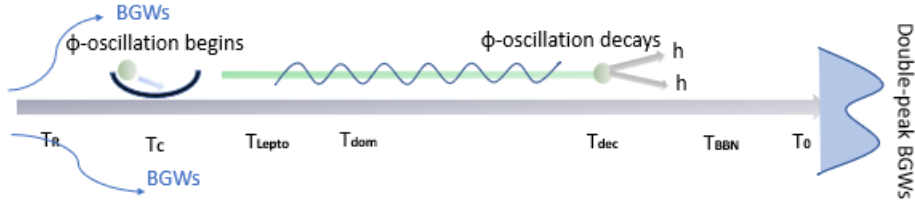


FIG. 1. A schematic timeline showing the occurrence of the events considered in this work. After inflation, the universe reheats at $T = T_R$. Phase transition happens, the scalar field oscillation begins, and RH neutrinos become massive at $T = T_c$. At the temperature $T_{\text{lepto}} \simeq M_N$, the baryon asymmetry produced by the RH neutrinos freezes out. Starting from T_{dom} until T_{dec} , the scalar field dominates the universe's energy density and produces entropy around $T \simeq T_{\text{dec}}$. The universe becomes radiation-dominated after this. The big-bang nucleosynthesis and the current temperature are denoted by T_{BBN} and T_0 , respectively. A peaked blue-tilted GW-spectrum generated during inflation when comes across such a dynamical phase of Φ , which also makes the RH neutrino massive and whose decay width is determined by the RH neutrino mass scale, becomes a double peak spectrum at present. The final spectrum carries imprints of the RH neutrino mass scale and, therefore, different regimes of leptogenesis.

context of the recent PTA results on nHz GWs and provide a rigorous statistical analysis of how the future GW detectors would be conjointly able to distinguish the flavour regimes by computing the signal-to-noise ratio (SNR). Finally, we draw our conclusions in Sec. V.

II. SCALAR FIELD DYNAMICS AND THE SCALE OF THERMAL LEPTOGENESIS

The Lagrangian relevant to the discussion is given by

$$-\Delta\mathcal{L} \subset f_{Di\alpha} \overline{N_{Ri}} \tilde{H}^\dagger L_\alpha + \frac{1}{2} f_{Ni} \overline{N_{Ri}} \Phi N_{Ri}^C + \frac{1}{4} \lambda_{H\Phi} |H|^2 |\Phi|^2 + V(\Phi, T), \quad (\text{II.1})$$

where f_D is the neutrino Dirac Yukawa coupling, $H(L)$ is the SM Higgs (lepton doublet), N_R is the RH neutrino field, Φ is a complex scalar field with vacuum expectation value v_Φ , and $V(\Phi, T)$ is the finite temperature potential that determines the phase transition dynamics of Φ . Here, N_R and L have $B - L$ charge -1 , whereas the same charges for Φ and H are 2 and 0, respectively. The Higgs portal coupling is in general given by $\lambda_{H\Phi} \simeq \lambda_{H\Phi}^{\text{tree}} + \lambda_{H\Phi}^{1\text{-loop}}$ where $\lambda_{H\Phi}^{1\text{-loop}}$ is generated by the first two terms in Eq. (II.1). We assume $\lambda_{H\Phi}^{\text{tree}} \lesssim \lambda_{H\Phi}^{1\text{-loop}}$ on all relevant physical scales which is crucial to establish a connection between the neutrino parameters and the lifetime of Φ . The RH neutrinos become massive ($M_i = f_{Ni} v_\Phi$) when Φ obtains its vacuum expectation value v_Φ . After the electroweak phase transition ($T \lesssim T_{\text{EW}}$), when the Higgs settles to its minima $H = v_h$, the first two terms generate light active neutrino mass $m_{\nu i} \sim f_{Di}^2 v_h^2 / M_i$ via the standard type-I seesaw mechanism [71–74], whereas at $T \gg T_{\text{EW}}$ the heavy neutrinos decay CP asymmetrically to lepton doublets plus Higgs, and generate lepton asymmetry. At a temperature $T \sim M_i$, lepton asymmetry produced by i th RH neutrino freezes out; therefore, M_i is typically the scale of thermal leptogenesis. For simplicity, not focusing so much on the hierarchy in M_i s, we consider a single scale for the rest of the discussion, i.e. $M_i \equiv M_N = f_N v_\Phi$. In the high-scale leptogenesis scenario, there are three distinct regimes of leptogenesis [60–62]. Generally, the RH neutrinos produce lepton doublets as a coherent superposition of flavours: $|L_i\rangle = A_{i\alpha} |L_\alpha\rangle$, where $\alpha = e, \mu, \tau$ and $A_{i\alpha}$ is the corresponding amplitude determined by $f_{Di\alpha}$. For temperatures $T \gtrsim 10^{12}$ GeV, all the charged lepton Yukawa

couplings are out of equilibrium (the interaction strength is given by $\Gamma_\alpha \sim 5 \times 10^{-3} f_{L\alpha} T$, with $f_{L\alpha}$ being the charged lepton Yukawa coupling) and do not participate in the leptogenesis process. This is the one flavour or the vanilla regime of leptogenesis (1FL). In this regime, leptogenesis is not sensitive to the neutrino mixing matrix, e.g. mixing angles and low-energy CP phases. When the temperature drops down to $T \lesssim 10^{12}$ GeV, the τ flavoured charged lepton interaction comes into equilibrium and breaks the coherent $|L_i\rangle$ state into τ and a composition of $e + \mu$ flavour (two flavour regime, 2FL). Likewise, the later composition is broken once $T \lesssim 10^9$ GeV, when the μ flavoured charged lepton interaction comes into equilibrium (three flavour regime, 3FL). In both these flavoured regimes, leptogenesis may be sensitive to the low-energy neutrino parameters. We will explore all these regimes and show that the flavoured regime of leptogenesis leaves much more distinct imprints on BGWs than the vanilla one, paving the path for a possible synergy between low-energy neutrino physics and GWs.

As the temperature drops, the scalar field transits from $\Phi = 0$ towards its vacuum expectation value $\Phi = v_\Phi$. The finite temperature potential that restores the symmetry at higher temperatures is given by [75–79]

$$V(\Phi, T) = D(T^2 - T_0^2)\Phi^2 - ET\Phi^3 + \frac{\lambda}{4}\Phi^4, \quad (\text{II.2})$$

with

$$D = \frac{3g'^2 + 4\lambda}{24}, \quad E = \frac{3g'^3 + g'\lambda + 3\lambda^{3/2}}{24\pi}, \quad T_0 = \frac{\sqrt{12\lambda}v_\Phi}{\sqrt{3g'^2 + 4\lambda}}, \quad (\text{II.3})$$

where g' is the gauge coupling,³ and the vacuum expectation value $v_\Phi = \mu/\sqrt{\lambda}$ has been determined from the zero temperature potential $V(\Phi, 0) = -\frac{\mu^2}{2}\Phi^2 + \frac{\lambda}{4}\Phi^4$. The structure of the finite temperature potential determines how the transition proceeds. The last term in Eq. (II.2) generates a potential barrier causing a secondary minimum at $\Phi \neq 0$, which at $T = T_c$ becomes degenerate with the $\Phi = 0$ one. At T_0 ($\lesssim T_c$), the potential barrier vanishes, making the minimum at $\Phi = 0$ a maximum [77]. The critical temperature T_c and the field value $\Phi_c = \Phi(T_c)$ are given by [77, 80]

$$T_c = T_0 \frac{\sqrt{\lambda D}}{\sqrt{\lambda D - E^2}}, \quad \Phi_c = \sqrt{\frac{4D}{\lambda}(T_c^2 - T_0^2)}. \quad (\text{II.4})$$

A non-zero value of E in Eq. (II.2) generally leads to a first-order transition with a strength determined roughly by the order parameter Φ_c/T_c [77]. Nonetheless, if $\Phi_c/T_c \ll 1$, the transition is extremely weakly first-order, which can be treated as a 'second-order' transition because the potential barrier disappears quickly ($T_c \simeq T_0$). In this case, the transition can be described by rolling of the field Φ from $\Phi = 0$ to $\Phi = v_\Phi$. In this article, we consider such a case working with the values of λ and g' so that $\Phi_c/T_c \ll 1$ is fulfilled. In particular, we find that, for $g'^3 \lesssim \lambda \lesssim 1$ and $g' \lesssim 10^{-2}$, the order parameter is $\Phi_c/T_c \lesssim 0.08$.⁴ Fixing the hierarchy between the couplings to be $\lambda \simeq g'^3$ (limiting condition), we also have $T_c \simeq T_0 = 2\sqrt{g'}v_\Phi$. Additionally, not to have a second period of inflation and for the field to roll, the conditions $\rho_\Phi(T_c) < \rho_R(T_c)$ and $m_\Phi = \sqrt{2\lambda}v_\Phi \gtrsim \mathcal{H}(T_c)$ must be satisfied, where ρ_i is the energy density and \mathcal{H} is the Hubble parameter. In terms of our model parameters, these conditions then translate to

$$\rho_\Phi(T_c) < 4.5 \times 10^{-6} \left(\frac{g'}{10^{-2}} \right) \rho_R(T_c), \quad \text{and} \quad \left(\frac{g'}{10^{-2}} \right)^{1/2} \gtrsim 4 \times 10^{-4} \left(\frac{v_\Phi}{10^{13} \text{ GeV}} \right), \quad (\text{II.5})$$

³ As mentioned in the introduction, seesaw models with $U(1)_{B-L}$ gauge symmetry is well-motivated from GUT. In that case, the scalar field carries a gauge charge. Therefore, the gauge coupling appears in the finite temperature potential.

⁴ In Ref.[3], it was checked numerically that the transition is a second-order type for this choice of parameters.

where the initial energy density of the scalar field is given by $\rho_\Phi(T_c) \simeq \lambda v_\Phi^4/4$.

Once the field rolls down to the true vacuum, it oscillates around v_Φ . For a generic potential $V(\Phi) = \alpha\Phi^\beta$, the equation of state of such a coherent oscillation can be computed as [3]

$$\omega = (\beta - 2)(\beta + 2)^{-1}. \quad (\text{II.6})$$

Assuming the oscillation of the scalar field is driven by the dominant quadratic term in the potential and expanding the zero temperature potential around the true vacuum, we obtain $\alpha = \lambda v_\Phi^2$ and $\beta = 2$. Therefore, the scalar field behaves like matter ($\omega = 0$). We can also compute the angular frequency of oscillation, which is $m_\Phi = \sqrt{2\lambda}v_\Phi$. If Φ is long-lived (lifetime set by the decay width as discussed below), these oscillations persist and the universe goes through a significant period of matter domination, thus leading to distinct imprints on the BGWs as we discuss later.

Let us now constrain the RH neutrino mass scale (scale of leptogenesis) $M_N = f_N v_\Phi$ and the decay width of Φ . First, the RH neutrino Yukawa coupling f_N should be large because we consider high-scale leptogenesis. However, in that case, if $m_\Phi > 2M_N$, Φ decay to RH neutrino pairs ($\Phi \rightarrow NN$) would be too quick to provide matter domination. Therefore, we restrict ourselves to the case $M_N \gtrsim m_\Phi$. Second, RH neutrinos become massive after the phase transition at $T = T_c$. Therefore, the scale of leptogenesis $T_{\text{lepto}} \sim M_N$ is bounded from above as $T_{\text{lepto}} \sim M_N \lesssim T_c$. For $\lambda \simeq g'^3$, the constraint $m_\Phi \lesssim M_N \lesssim T_c$ from requiring long-lived Φ and successful leptogenesis thus becomes⁵

$$\sqrt{2g'g'} \lesssim f_N \lesssim 2\sqrt{g'}. \quad (\text{II.7})$$

Notice that in this specific case, the mass of Φ is suppressed by a factor $\sqrt{g'}$ compared to the $M_{Z'} = \sqrt{2}g'v_\Phi$, thus kinematically forbidding the Φ decays into Z' pairs.

Two competitive decay channels of Φ are now $\Phi \rightarrow hh$ and $\Phi \rightarrow f\bar{f}V$, where h , f , and V are the SM Higgs, leptons and vector bosons, respectively (more about Φ decays are discussed at the end of this section). Both the decays are radiative and therefore suppressed, making Φ long-lived. The first decay channel, $\Phi \rightarrow hh$, is mediated by the neutrino Dirac Yukawa f_D and the coupling f_N (see Fig. 2). Hence, it is directly connected to light neutrino and leptogenesis parameter space, making it the main decay channel in our study. In the limit $m_\Phi \gg m_h$, the decay rate is given by [81–83]

$$\Gamma_\Phi^{hh} \simeq \frac{(\lambda_{H\Phi}^{1\text{-loop}})^2 v_\Phi^2}{32\pi m_\Phi} \simeq \Gamma_0 \frac{f_N^6}{\lambda} \left(\frac{v_\Phi}{10^{13} \text{ GeV}} \right)^2 \left(\frac{m_\Phi}{10^8 \text{ GeV}} \right) \ln^2 \left(\frac{\Lambda}{\mu} \right), \quad (\text{II.8})$$

where the one-loop effective coupling $\lambda_{H\Phi}^{1\text{-loop}} \sim f_D^2 f_N^2 / (2\pi^2) \ln(\Lambda/\mu)$ with $f_D = \sqrt{m_\nu f_N v_\Phi / v_h^2}$ has been evaluated for $m_\nu \simeq 0.01$ eV plus $v_h = 174$ GeV, and $\Gamma_0 \simeq 1.3 \times 10^{-2}$. The logarithmic factor accounts for the renormalization condition such that at a very high scale, e.g. at $\Lambda \equiv \Lambda_{\text{GUT}} \simeq 10^{16}$ GeV,⁶ the 1-loop portal coupling vanishes, and μ is a relevant physical scale. Considering $\mathcal{H} \simeq \Gamma_\Phi^{hh}$ we can now compute T_{dec} as

$$T_{\text{dec}} = \tilde{T}_{\text{dec}} \ln \left(\frac{\Lambda}{\mu} \right), \quad (\text{II.9})$$

where

$$\tilde{T}_{\text{dec}} = \left(\frac{90}{\pi^2 g_*} \right)^{1/4} \left[\tilde{M}_{\text{Pl}} \Gamma_0 \frac{f_N^6}{\lambda} \left(\frac{v_\Phi}{10^{13} \text{ GeV}} \right)^2 \left(\frac{m_\Phi}{10^8 \text{ GeV}} \right) \right]^{1/2}, \quad (\text{II.10})$$

⁵ In numerical computation, we shall consider a bit stronger upper limit: $f_N \lesssim g'^{3/4}$, by neglecting the contribution of the terms $\mathcal{O}(f_N^4)$ in the effective potential.

⁶ Note that Λ is a free scale. For phenomenological purposes, it is therefore sufficient to consider non-vanishing effective coupling at low energies to obtain matter domination and consequently detectable spectral distortion in the GWs. In our scenario, $\Lambda \simeq T_{\text{lepto}} \gtrsim m_\Phi$ would not change the result significantly because the dependence is logarithmic. We can therefore also safely neglect any Higgs portal physics at temperatures $T \gtrsim T_{\text{lepto}} \gtrsim m_\Phi$.

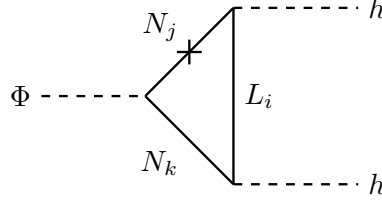


FIG. 2. Diagram generating leading-order radiative ΦHH coupling through RH neutrino and Lepton mediation [81–84].

with $\tilde{M}_{\text{Pl}} = 2.4 \times 10^{18}$ GeV being the reduced Planck constant, and $g_* \simeq 106.75$ the effective degrees of freedom that contribute to the radiation. For the physical scale $\mu \equiv T_{\text{dec}}$, the solution to Eq. (II.9) is given by

$$T_{\text{dec}} = \tilde{T}_{\text{dec}} \mathcal{W}\left(\frac{\Lambda}{\tilde{T}_{\text{dec}}}\right), \quad (\text{II.11})$$

where $\mathcal{W}(\Lambda/\tilde{T}_{\text{dec}})$ is a Lambert function that modulates the T_{dec} owing to the imposed renormalisation condition. The Lambert function and the coupling f_N have opposite effects on T_{dec} . The former tends to increase T_{dec} because $\mathcal{W}(\Lambda/\tilde{T}_{\text{dec}}) \gg 1$ for $\Lambda \gg \tilde{T}_{\text{dec}}$ (which is the case in our scenario), whereas a decrease in the latter results in a decrease in T_{dec} . However, since the quantity \tilde{T}_{dec} goes as f_N^3 , the latter effect is much stronger. In addition to the conditions described in Eq.s (II.5) and (II.7), a viable parameter space of the framework must also comply with the following constraints: first, the scalar field should decay before the BBN, i.e., $T_{\text{dec}} \gtrsim T_{\text{BBN}} \sim 10$ MeV; second, the channel $\Phi \rightarrow hh$ has to dominate over $\Phi \rightarrow f\bar{f}V$ (we need the matter-dominated epoch driven by Φ to be determined by the neutrino parameters), i.e., $\Gamma_{\Phi}^{hh} \gtrsim \Gamma_{\Phi}^{f\bar{f}V}$, where $\Gamma_{\Phi}^{f\bar{f}V}$ is given by [84]

$$\Gamma_{\Phi}^{f\bar{f}V} \simeq \lambda g'^4 \left(\frac{m_{\Phi}}{10^8 \text{ GeV}}\right). \quad (\text{II.12})$$

Given the above constraints, we now extract the viable parameter space of our model and compute the quantities T_{dec} , T_{dom} and the entropy production factor κ which are most relevant to describe the spectral features in the BGWs discussed in the next section. In the computation of GW spectra, we use analytical expressions for these quantities. While T_{dec} is defined in Eq. (II.11), the other two are given by

$$T_{\text{dom}} = \frac{\rho_{\Phi}(T_c)}{\rho_R(T_c)} T_c, \quad \text{and} \quad \kappa = \frac{T_{\text{dom}}}{T_{\text{dec}}} \Theta [T_{\text{dom}} - T_{\text{dec}}], \quad (\text{II.13})$$

where the Θ function represents that the expression for κ is valid for $T_{\text{dom}} > T_{\text{dec}}$ only.

To crosscheck the accuracy of the analytical results and to track the evolution of the energy densities and the entropy production as a function of the temperature (see e.g. the right panel of Fig. 3), it is useful to solve the following Friedmann equations for the energy densities:

$$\frac{d\rho_R}{dt} + 4\mathcal{H}\rho_R = \Gamma_{\Phi}^{hh} \rho_{\Phi}, \quad \frac{d\rho_{\Phi}}{dt} + 3\mathcal{H}\rho_{\Phi} = -\Gamma_{\Phi}^{hh} \rho_{\Phi}, \quad \frac{ds}{dt} + 3\mathcal{H}s = \Gamma_{\Phi}^{hh} \frac{\rho_{\Phi}}{T}, \quad (\text{II.14})$$

upon recasting them as

$$\frac{d\rho_R}{dz} + \frac{4}{z}\rho_R = 0, \quad \frac{d\rho_{\Phi}}{dz} + \frac{3}{z}\frac{\mathcal{H}}{\tilde{\mathcal{H}}}\rho_{\Phi} + \Gamma_{\Phi}^{hh} \frac{1}{z\tilde{\mathcal{H}}}\rho_{\Phi} = 0, \quad (\text{II.15})$$

Benchmark cases	M_N [GeV]	f_N	v_Φ [GeV]	T_{dom} [GeV]	T_{dec} [GeV]	κ
BP1 (1FL)	1.4×10^{12}	2.0×10^{-3}	7.0×10^{14}	6.4×10^8	9.8×10^7	6.5
BP2 (2FL)	1.6×10^{10}	1.4×10^{-3}	1.1×10^{13}	1.0×10^7	1.0×10^5	1.0×10^2
BP3a (3FL)	1.3×10^8	3.4×10^{-3}	3.9×10^{10}	3.4×10^4	3.4×10^2	1.0×10^2
BP3b (3FL)	1.3×10^8	1.4×10^{-3}	9.5×10^{10}	8.6×10^4	9.7×10^1	8.9×10^2

TABLE I. The four benchmark points considered in this paper. In each case, leptogenesis occurs in the standard radiation domination because $T_{\text{lepto}} \sim M_N > T_{\text{dom}}$, where T_{dom} is the temperature at which the scalar field starts to dominate.

where $z = T_c/T$, s is the entropy density of the thermal bath, and from the third of Eq. (II.14), the temperature-time relation has been derived as

$$\frac{1}{T} \frac{dT}{dt} = - \left(\mathcal{H} + \frac{1}{3g_{*s}(T)} \frac{dg_{*s}(T)}{dt} - \Gamma_\Phi^{hh} \frac{\rho_\Phi}{4\rho_R} \right) = -\tilde{\mathcal{H}}. \quad (\text{II.16})$$

On the other hand, the amount of entropy production from the Φ decays can be computed by solving

$$\frac{da}{dz} = \left(1 + \Gamma_\Phi^{hh} \frac{\rho_\Phi}{4\rho_R \tilde{\mathcal{H}}} \right) \frac{a}{z}, \quad (\text{II.17})$$

with a being the scale factor, and then computing the ratio of $\tilde{S} \sim a^3/z^3$, i.e., $\kappa = \tilde{S}_{\text{after}}/\tilde{S}_{\text{before}}$.

In the most general setting, our model has four independent parameters which are the Φ vacuum expectation value v_Φ and the three couplings f_N , λ and g' (or equivalently the three masses M_N , m_Φ and $M_{Z'}$). However, for the sake of definiteness, we hereafter assume $\lambda \simeq g'^3$ which is the limiting condition to achieve a second-order phase transition. Concerning the gauge coupling, although we do not specify any GUT scheme, large values of g' are generally desirable for realistic GUT scenarios. In the main analysis, we discuss the results for $g' = 10^{-2}$ that captures the qualitative features of the parameter space. In the Appendix A, we investigate the impact of varying g' within an order of magnitude and show that for an appreciable range of g' , the qualitative results of our analysis remain the same.

In Fig. 3 we show the produced entropy on the allowed model parameter space (left plot) and the evolution of the normalised energy densities $\Omega_i = \rho_i/\rho_{\text{tot}}$ and the entropy⁷ (right plot) for the four sets of benchmark parameters (see Tab. I). The benchmark points are chosen such that each falls into a specific regime of leptogenesis: BP (1, 2, 3) are in 1FL, 2FL, and 3FL regimes, respectively. Note that BP3a and BP2 fall into the category of equal entropy production. Despite this, as shown in the next section, they exhibit different spectral features because they correspond to different $T_{\text{dec}(\text{dom})}$. On the other hand, BP3b corresponds to the largest entropy production in this model which is exclusive only to the 3FL and produces a very distinct GW signal.

In the left panel of Fig. 3, the Yukawa coupling f_N is bounded from above and below. The lower bound comes from Eq. (II.7) while the upper bound corresponds to $f_N^4 \lesssim g'^3$ because we neglected the terms $\mathcal{O}(f_N^4)$ in the effective potential. This is a bit stronger upper bound than the one shown in Eq. (II.7). The white triangular region on the top is excluded because $T_{\text{dom}} < T_{\text{dec}}$ ($\kappa < 1$), which is unphysical. The region below the dot-dashed line corresponds to $\Gamma_\Phi^{fV} > \Gamma_\Phi^{hh}$ which is excluded. The region on the right of the short-dashed line is instead excluded since v_Φ is larger

⁷ We have also checked that the analytical expression for the entropy production factor κ in Eq. (II.13) matches the numerical result (Fig. 3, right) with good accuracy.

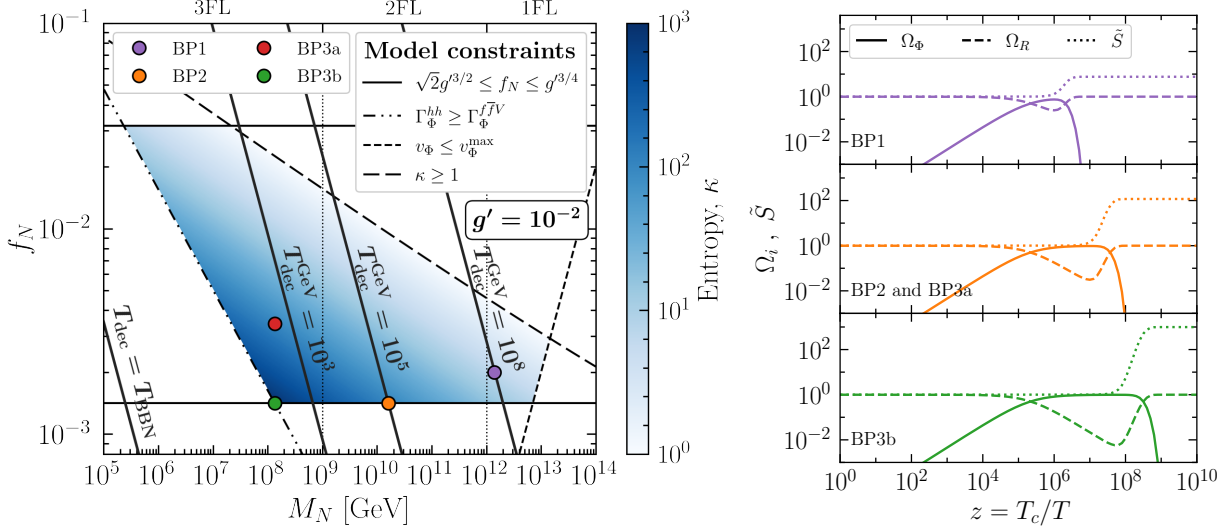


FIG. 3. Left: The entropy produced (κ) by the Φ decays on the M_N - f_N plane for $g' = 10^{-2}$. The white regions are excluded by the different constraints represented by the thin black lines (for more details see Sec. II). The oblique thick black lines are contours for different values of T_{dec} (in units of GeV), while the dotted vertical lines highlight the transition among the different flavour regimes of leptogenesis. The four points correspond to the four benchmark cases reported in Tab. I. Right: the evolution of the normalized energy density $\Omega_i = \rho_i/\rho_{\text{tot}}$ for Φ scalar (solid lines) and radiation (dashed lines), and the total entropy (dotted lines) as a function of the auxiliary variable z . The three panels are for the benchmark points shown in the left plot. The benchmark points BP2 and BP3a share the same plots since the ratios among the temperatures T_c , T_{dom} and T_{dec} are the same (see also Tab. I). Because only the ratio of the entropy after and before the decay is important, the initial value of \tilde{S} has been chosen as $\tilde{S}(z=1) = 1$. The parameter κ in Eq. (II.13) is therefore $\kappa = \tilde{S}_{\text{after}} = \tilde{S}(z \rightarrow \infty)$.

than $v_{\Phi}^{\max} \simeq 5 \times 10^{15}$ GeV $\lesssim \Lambda_{\text{GUT}}$. The parameter space presented in Fig. 3 is also consistent with the other two constraints reported in Eq. (II.5). The oblique black thick lines correspond to different decay temperatures. Notice that the different flavour regimes of leptogenesis correspond to very distinct ranges for T_{dec} which are: $T_{\text{dec}} \lesssim 10^3$ GeV for 3FL, 10^5 GeV $\lesssim T_{\text{dec}} \lesssim 10^8$ GeV for 2FL, and $T_{\text{dec}} \gtrsim 10^8$ GeV for 1FL. As we will show later, this distinction will be more pronounced when looking at the spectral distortion in the GWs.

We conclude this section with the following remarks. First, as we shall see in the next section, larger entropy production corresponds to more prominent spectral distortion in the GWs. Therefore, the region around $M_N \simeq m_{\Phi}$ is the best parameter space of this model. Second, this paper does not present any detailed computation related to the baryon asymmetry. We however note that the baryon asymmetry produced by the RH neutrinos will be diluted due to the entropy injection given in Eq. (II.13). Therefore, unlike the conventional choice of a strong hierarchy in the RH neutrino masses, a more suitable option would be to make RH neutrinos quasi-degenerate. This not only evades the issue of entropy dilution by enhancing the baryon asymmetry via the resonant-leptogenesis mechanism [51], but also justifies our choice of a single RH neutrino mass scale $M_i \equiv M_N$ throughout. We can get an order of magnitude estimate on the level of quasi-degeneracy in the RH neutrinos. The produced baryon-to-photon ratio in the resonance regime can be written as [51]

$$\eta_B = 10^{-2} \varepsilon_i \zeta_i \kappa^{-1} \quad \text{with} \quad \varepsilon_i \simeq \frac{3M_i m_{\nu}}{8\pi v_h^2 \delta}, \quad (\text{II.18})$$

where ε_i is the CP asymmetry parameter, $\zeta_i \simeq 10^{-1}$ is the efficiency of lepton asymmetry production, $\delta = (M_j - M_i)/M_i$, and κ is the injected entropy by Φ decay as defined in Eq. (II.13). We can obtain an expression for δ in two cases. The standard case without entropy production corresponds to $\kappa = 1$. Given the observed value $\eta_B \simeq 6.3 \times 10^{-10}$ [85], using Eq. (II.18), we obtain

$$\delta_S \simeq 6.25 \times 10^{-1} \left(\frac{M_N}{10^9 \text{GeV}} \right), \quad \delta_E \simeq \delta_S \kappa^{-1}, \quad (\text{II.19})$$

$$(\text{II.20})$$

where the subscript $S(E)$ represents the mass splitting in the standard (with entropy production) case. Therefore, e.g., for BP3b, we get δ_E to be three orders of magnitude (see the value of κ in Tab. I) less than the standard case. Second, we assume $\lambda_{H\Phi}^{1\text{-loop}} \gtrsim \lambda_{H\Phi}^{\text{tree}}$ for the thermal history to be determined by the neutrino parameters. Therefore, for our scenario to work, we must have

$$\lambda_{H\Phi}^{\text{tree}} \lesssim \left[\Gamma_{\Phi}^{hh} \frac{32\pi m_{\Phi}}{v_{\Phi}^2} \right]^{1/2}. \quad (\text{II.21})$$

Using Eq. (II.8) and the chosen values of f_N , e.g., for BP2 (BP3a), we have $\lambda_{H\Phi}^{\text{tree}} \lesssim 10^{-11(12)}$. This shows that, in either case, the $B - L$ scalar must be feebly coupled with the SM Higgs at the tree level. Finally, let us also remark that, while virtual Z' mediated 1-loop decays of Φ to two fermion final states are chirality suppressed [84, 86] compared to $\Phi \rightarrow f\bar{f}V$, N_R and Z' mediated 1-loop decays with N_R and Z' s at the final states are not allowed because of the constraint in Eq. (II.7). Another potentially interesting decay channel $\Phi \rightarrow ZZ$ might pop up due to kinetic mixing between $U(1)_Y$ and $B - L$ gauge bosons. In the $U(1)_{B-L}$ model, the minimum size of the kinetic mixing obtained at 1-loop level is given by $\epsilon \sim gg'/16\pi^2$ (up to some logarithmic factor imposed by the renormalization condition) [87–89], where g and g' are the couplings of two $U(1)$'s. Therefore for large $U(1)_{B-L}$ coupling, ϵ could be large—in fact, this is the reason that kinetic mixing imposes significant restriction on the parameter space of low mass Z' searches [90]. In our case, however, Z' is extremely heavy and mixes with the SM gauge boson eigenstate with a strength $\alpha \sim \sin\theta_W \epsilon (m_Z/M_{Z'})^2$, where θ_W is the weak mixing angle. Because of this suppressed mixing, even for $g' \sim 10^{-2}$, the induced $\Phi\Phi ZZ$ coupling is much weaker than that of $\Phi\Phi hh$ used in our analysis. But this effect could be considerable in a top-down model (e.g. if the model predicts large g' and small vacuum expectation value of the $B - L$ scalar).

III. IMPRINTS OF FLAVOUR REGIMES OF LEPTOGENESIS ON BGWS

In what follows, we briefly discuss the GW production during inflation and their propagation through multiple cosmological epochs until today. The perturbed FLRW line element that describes GWs is given by

$$ds^2 = a(\tau) \left[-d\tau^2 + (\delta_{ij} + h_{ij})dx^i dx^j \right], \quad (\text{III.1})$$

where τ is the conformal time, and $a(\tau)$ is the scale factor. The transverse and traceless ($\partial_i h^{ij} = 0$, $\delta^{ij} h_{ij} = 0$) part of h_{ij} represents the GWs. Because the GWs are weak, $|h_{ij}| \ll 1$, the following linearized evolution equation

$$\partial_{\mu}(\sqrt{-g}\partial^{\mu}h_{ij}) = 16\pi a^2(\tau)\pi_{ij} \quad (\text{III.2})$$

is sufficient to study the propagation of the GWs. The quantity π_{ij} represents an anisotropy stress tensor that couples to h_{ij} as an external source, which within a realistic cosmic setting

only affects the GWs at large scales (than those of PTAs), e.g., due to the free streaming of light neutrinos [91, 92]. The Fourier space decomposition of h_{ij} reads

$$h_{ij}(\tau, \vec{x}) = \sum_{\lambda} \int \frac{d^3\vec{k}}{(2\pi)^{3/2}} e^{i\vec{k}\cdot\vec{x}} \epsilon_{ij}^{\lambda}(\vec{k}) h_k^{\lambda}(\tau), \quad (\text{III.3})$$

where the index $\lambda = “+ / -”$ represents two polarisation states. The polarisation tensor $\epsilon_{ij}^{\lambda}(\vec{k})$ besides being transverse and traceless, complies with the following conditions: $\epsilon^{(\lambda)ij}(\vec{k})\epsilon_{ij}^{(\lambda')}(\vec{k}) = 2\delta_{\lambda\lambda'}$ and $\epsilon_{ij}^{(\lambda)}(-\vec{k}) = \epsilon_{ij}^{(\lambda)}(\vec{k})$. Assuming isotropy and similar evolution of each polarisation state, we replace $h_k^{\lambda}(\tau)$ with $h_k(\tau)$, where $k = |\vec{k}| = 2\pi f$ with f being the present frequency at $a_0 = 1$. Neglecting subdominant contribution from π_{ij} , the GW propagation equation in the Fourier space reads

$$\ddot{h}_k + 2\frac{\dot{a}}{a}\dot{h}_k + k^2 h_k = 0, \quad (\text{III.4})$$

where the dot represents a conformal time derivative. Using Eq. (III.3) and Eq. (III.4), the energy density of the GWs can be computed as [93]

$$\rho_{\text{GW}} = \frac{1}{32\pi G} \int \frac{dk}{k} \left(\frac{k}{a}\right)^2 T_T^2(\tau, k) P_T(k), \quad (\text{III.5})$$

where $T_T^2(\tau, k) = |h_k(\tau)|^2/|h_k(\tau_i)|^2$ is a transfer function with τ_i as the initial conformal time. The quantity $P_T(k) = k^3|h_k(\tau_i)|^2/\pi^2$ characterizes the primordial power spectrum and connects to the inflation models with specific forms. Here we opt for a power-law parametrization of P_T :

$$P_T(k) = r A_s(k_*) \left(\frac{k}{k_*}\right)^{n_T}, \quad (\text{III.6})$$

where $r \lesssim 0.06$ [94] is the tensor-to-scalar-ratio, and $A_s \simeq 2 \times 10^{-9}$ is the scalar perturbation amplitude at the pivot scale $k_* = 0.01 \text{ Mpc}^{-1}$. In the present analysis, we take $r = 0.06$ and consider the tensor spectral index n_T constant plus blue-tilted ($n_T > 0$). However, a scale dependence might arise owing to the higher order corrections [95, 96] depending on the inflation model, which we do not discuss here.⁸ The normalized GW energy density pertinent to detection purposes is expressed as

$$\Omega_{\text{GW}}(k) = \frac{k}{\rho_c} \frac{d\rho_{\text{GW}}}{dk}, \quad (\text{III.7})$$

where $\rho_c = 3\mathcal{H}_0^2/8\pi G$ with $\mathcal{H}_0 \simeq 2.2 \times 10^{-4} \text{ Mpc}^{-1}$ being the Hubble constant. From Eq. (III.5), the quantity $\Omega_{\text{GW}}(k)$ is derived as

$$\Omega_{\text{GW}}(k) = \frac{1}{12\mathcal{H}_0^2} \left(\frac{k}{a_0}\right)^2 T_T^2(\tau_0, k) P_T(k), \quad \tau_0 = 1.4 \times 10^4 \text{ Mpc}. \quad (\text{III.8})$$

The transfer function can be computed analytically, matching numerical results with a fair accuracy [98–103]. When an intermediate matter domination (recall that a RH neutrino mass-dependent intermediate matter domination is the central theme of this article) is at play, $T_T^2(\tau_0, k)$ can be calculated as [102, 103]

$$T_T^2(\tau_0, k) = F(k) T_1^2(\zeta_{\text{eq}}) T_2^2(\zeta_{\Phi}) T_3^2(\zeta_{\Phi R}) T_2^2(\zeta_R), \quad (\text{III.9})$$

⁸ We point out that the single field slow-roll inflation models correspond to the consistency relation $n_T = -r/8$ [97], i.e., the spectral index is slightly red-tilted ($n_T \lesssim 0$).

where the individual transfer functions read as

$$T_1^2(\zeta) = 1 + 1.57\zeta + 3.42\zeta^2, \quad (\text{III.10})$$

$$T_2^2(\zeta) = (1 - 0.22\zeta^{1.5} + 0.65\zeta^2)^{-1}, \quad (\text{III.11})$$

$$T_3^2(\zeta) = 1 + 0.59\zeta + 0.65\zeta^2, \quad (\text{III.12})$$

with $\zeta_i = k/k_i$. The modes k_i given by

$$k_{\text{eq}} = 7.1 \times 10^{-2} \Omega_m h^2 \text{Mpc}^{-1} \text{ with } \Omega_m = 0.31, \quad h = 0.7, \quad (\text{III.13})$$

$$k_\Phi = 1.7 \times 10^{14} \left(\frac{g_{*s}(T_{\text{dec}})}{106.75} \right)^{1/6} \left(\frac{T_{\text{dec}}}{10^7 \text{GeV}} \right) \text{Mpc}^{-1}, \quad (\text{III.14})$$

$$k_{\Phi R} = 1.7 \times 10^{14} \kappa^{2/3} \left(\frac{g_{*s}(T_{\text{dec}})}{106.75} \right)^{1/6} \left(\frac{T_{\text{dec}}}{10^7 \text{GeV}} \right) \text{Mpc}^{-1}, \quad (\text{III.15})$$

$$k_R = 1.7 \times 10^{14} \kappa^{-1/3} \left(\frac{g_{*s}(T_R)}{106.75} \right)^{1/6} \left(\frac{T_R}{10^7 \text{GeV}} \right) \text{Mpc}^{-1}, \quad (\text{III.16})$$

re-enter the horizon at T_{eq} (the standard matter-radiation equality temperature), at T_{dec} (the temperature at which the scalar field decays), at T_{dom} (the temperature at which the scalar field starts to dominate) and at T_R (when the universe reheats after inflation), respectively. In our computation, we use the analytical expression for κ presented in Eq. (II.13). Notice that we have to consider the reheating after inflation precedes the phase transition of Φ , i.e., $T_R > T_c$ which does not contradict the condition for thermal leptogenesis $T_R > M_N$ because $T_c > M_N$ (see Eq. (II.7)). In the numerical analysis, we shall discuss the results for $T_c \lesssim T_R \lesssim T_R^{\text{max}}$, where we consider $T_R^{\text{max}} \simeq 10^{15}$ GeV as the maximum allowed reheating temperature. The quantity $F(k)$ in Eq. (III.9) is given by

$$F(k) = \Omega_m^2 \left(\frac{g_*(T_{k,\text{in}})}{g_{*0}} \right) \left(\frac{g_{*0s}}{g_{*s}(T_{k,\text{in}})} \right)^{4/3} \left(\frac{3j_1(k\tau_0)}{k\tau_0} \right)^2, \quad (\text{III.17})$$

where $T_{k,\text{in}}$ is the temperature corresponding to the horizon entry of the k th mode, $j_1(k\tau_0)$ is the spherical Bessel function, $g_{*0} = 3.36$, $g_{*0s} = 3.91$, and an approximate form of the scale-dependent g_* is given by [103–105]

$$g_{*(s)}(T_{k,\text{in}}) = g_{*0(s)} \left(\frac{A + \tanh k_1}{A + 1} \right) \left(\frac{B + \tanh k_2}{B + 1} \right), \quad (\text{III.18})$$

where

$$A = \frac{-1 - 10.75/g_{*0(s)}}{-1 + 10.75/g_{*0(s)}}, \quad B = \frac{-1 - g_{\text{max}}/10.75}{-1 + g_{\text{max}}/10.75}, \quad (\text{III.19})$$

and

$$k_1 = -2.5 \log_{10} \left(\frac{k/2\pi}{2.5 \times 10^{-12} \text{ Hz}} \right), \quad k_2 = -2.0 \log_{10} \left(\frac{k/2\pi}{6.0 \times 10^{-9} \text{ Hz}} \right), \quad (\text{III.20})$$

with g_{max} being $\simeq 106.75$. With the above set of equations, we evaluate the normalized GW energy density $\Omega_{\text{GW}}(k)$ in Eq. (III.8) for the benchmark parameters considered in the previous section and reported in Tab. I. Before we present the numerical results, let us point out that the quantity $\Omega_{\text{GW}}(k)h^2$ is constrained by two robust bounds on the Stochastic Gravitational Wave Background

(SGWB) placed by the effective number of relativistic species during Big Bang Nucleosynthesis (BBN) [106] and by the LIGO measurements [107]. In particular, the BBN constraint reads

$$\int_{f_{\text{low}}}^{f_{\text{high}}} df f^{-1} \Omega_{\text{GW}}(f) h^2 \lesssim 5.6 \times 10^{-6} \Delta N_{\text{eff}}, \quad (\text{III.21})$$

with $\Delta N_{\text{eff}} \lesssim 0.2$. The lower limit of the integration is the frequency that represents the mode entering the horizon at the BBN epoch, which we take as $f_{\text{low}} \simeq 10^{-10}$ Hz. We consider the upper limit $f_{\text{high}} \simeq 10^7$ Hz corresponding to $T_R \equiv T_R^{\text{max}} \simeq 10^{15}$ GeV. For the LIGO constraint, we rely on a crude estimation by considering a reference frequency $f_{\text{LIGO}} = 25$ Hz and discarding the GWs having an amplitude more than 8.33×10^{-9} at f_{LIGO} [108]. On the other hand, in case of currently unconstrained GW signals, we quantitatively assess their detectability by next-generation detectors after $t_{\text{obs}} = 1$ yr observing time by computing the signal-to-noise ratio (SNR) defined as [109, 110]

$$\text{SNR} = \sqrt{t_{\text{obs}} \int_{f_{\text{min}}}^{f_{\text{max}}} df \left(\frac{\Omega_{\text{GW}}(f)}{\Omega_{\text{noise}}(f)} \right)^2}, \quad (\text{III.22})$$

where $\Omega_{\text{noise}}(f)$ is the noise spectrum of the detector and $f_{\text{min}}(f_{\text{max}})$ are minimum (maximum) accessible frequency.

IV. RESULTS

In this section, we present our numerical results on the spectral features in the BGW spectra and quantitatively assess their potential detection in future experiments. We consider the case of $g' = 10^{-2}$ and discuss the impact of the different values for the gauge coupling in the Appendix A, where we demonstrate that our results are qualitatively unchanged.

In Figs 4 and 5, we present the normalized GW energy density as a function of the frequency and the spectral features of the BGWs induced by the Φ matter domination set by the RH neutrino mass scale for different values of tensor spectral index n_T . These figures differ from the assumption on the reheating temperature T_R which is taken to be T_c and $T_R^{\text{max}} = 10^{15}$ GeV, respectively. In both figures, the different panels correspond to the four leptogenesis benchmark points presented in Tab. I. The GW spectra are characterized by three frequencies, $f_{\text{low}}^{\text{peak}}$, f^{dip} , and $f_{\text{high}}^{\text{peak}}$, which correspond to the temperatures T_{dec} , T_{dom} , and T_R (cf Eq.s (III.14), (III.15) and (III.16)). Notice that irrespective of the spectral index n_T , the overall spectrum gets more suppressed for large entropy production. In addition, the red tilt in the middle becomes more prominent because longer duration of Φ domination delays the horizon entry of scales $k^{-1} \in [k_{\Phi}^{-1}, k_{\Phi R}^{-1}]$, and the corresponding amplitude within these k values get reduced. Therefore, as the RH neutrino mass scale decreases (e.g. going from BP1 to BP3), we get a more distinct double-peaked spectrum in case of $T_R = T_c$. As such, a three-flavour leptogenesis scenario (BP3b: bottom-right panel) can predict a more distinct double peak spectrum than a two-flavour (BP2: top-right panel) or one-flavour (BP1: top-left panel) scenario. Note also that though the spectral distortion, i.e., the ratio $\Omega_{\text{GW}}(f_{\text{low}}^{\text{peak}})/\Omega_{\text{GW}}(f^{\text{dip}})$ is same for BP2 and BP3a, the peak and the dip frequencies are in different position as $T_{\text{dec}(\text{dom})}$ is different for these benchmark points. In addition to that, starting from a one-flavour/vanilla regime, as a leptogenesis scenario goes deep into the flavour regime, the low-frequency peak and the dip shift towards lower frequencies. As evident from Fig. 4, these frequencies (two-flavour scenario) fall within the LISA-DECIGO (mHz-Hz) sensitivity [36, 39], whereas, for BP3 (three-flavour scenario), it falls in the mHz- μ Hz region.

In Fig. 6, we translate the BBN (solid lines) and LIGO (dashed lines) constraints on Ω_{GW} into bounds on the model parameters and, remarkably, on the RH neutrino mass scale. These

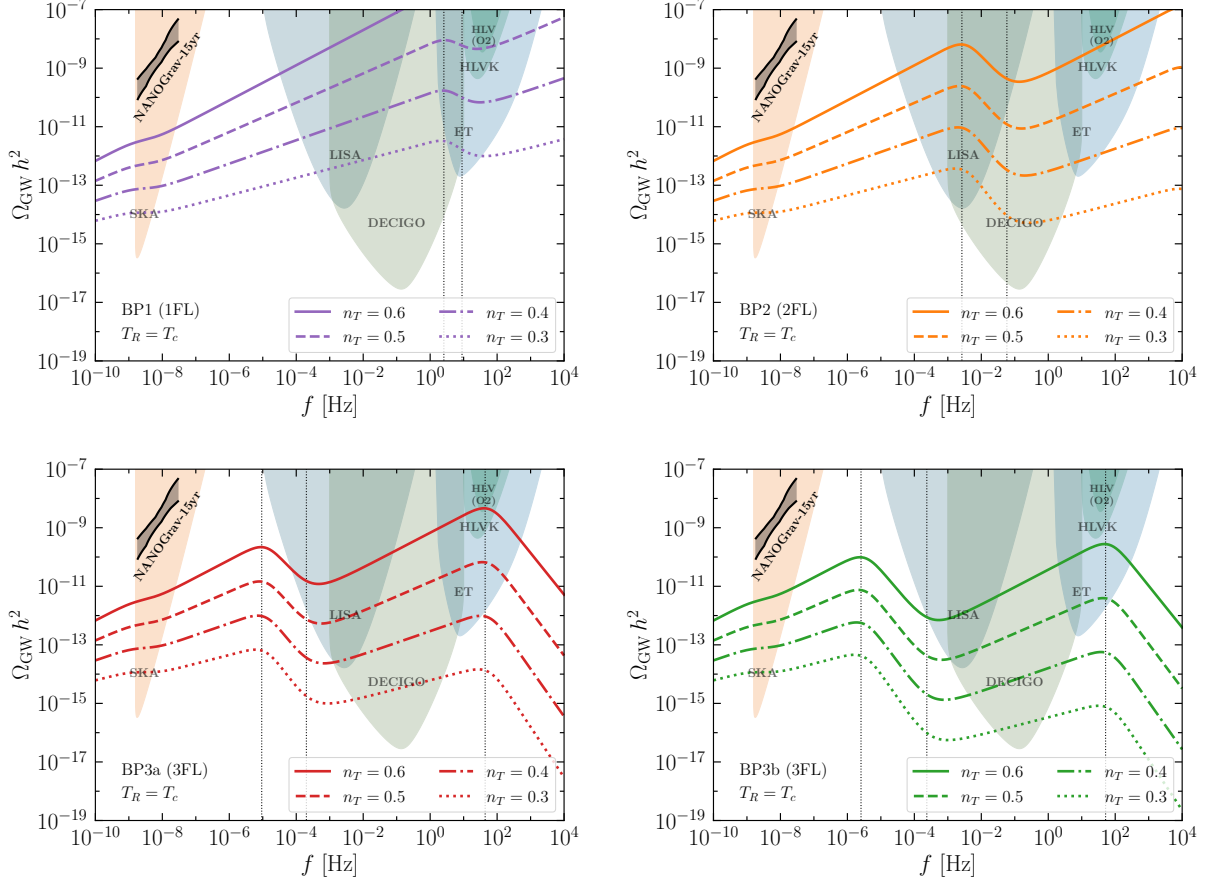


FIG. 4. BGW spectra in case of four different values of the tensor spectral index n_T , assuming $T_R = T_c$. The different plots correspond to the four benchmark points (given in Tab. I) depicting different entropy production and flavour regimes of leptogenesis. The shaded regions are sensitivity curves of various GW experiments such as SKA [33], LISA [37], DECIGO [40], ET [42], and HLVK [45]. The black bands in the nHz region represents the NANOGrav 15yrs data posteriors [6]. The dotted vertical lines (from left to right) correspond to $f_{\text{low}}^{\text{peak}}$, f_{dip} , and $f_{\text{high}}^{\text{peak}}$, respectively.

constraints depend on the value of the tensor spectral index n_T (different colored lines) and on the reheating temperature of the universe for which we consider the two opposite cases: $T_R = T_c$ (left panel) and $T_R = T_R^{\text{max}} = 10^{15}$ GeV (right panel). Notice that the parameter space to the right of the displayed lines is excluded. In case of $T_R = T_c$, we find the most conservative limits and the LIGO constraint to be in general much stronger than BBN one, ruling out almost the entire parameter space under consideration for $n_T = 0.7$. On the other hand, the case $T_R = T_R^{\text{max}}$ correspond to the strongest limits on the model parameter space, which is completely ruled out for $n_T = 0.6$. The allowed parameter space opens for smaller values of n_T . We find that the three-flavour and two-flavour regimes are allowed in case of $n_T \lesssim 0.6$ and $n_T \lesssim 0.5$ for $T_R = T_c$ and $T_R = T_R^{\text{max}}$, respectively. For $n_T \ll 0.5$, most of the model parameter space evades instead all the GW bounds. An important aspect of the obtained GW spectrum is that the overall amplitude increases with n_T , and the spectrum spans a wide range of frequencies. Therefore, one way to predict robustly testable GW signals is to fix a UV model that would predict a particular value of n_T ($\ll 0.7$ for the flavoured leptogenesis model as discussed here), which is not our approach. Another way, which we discuss here, is to take an IR approach by being agnostic about the source of the BGWs and

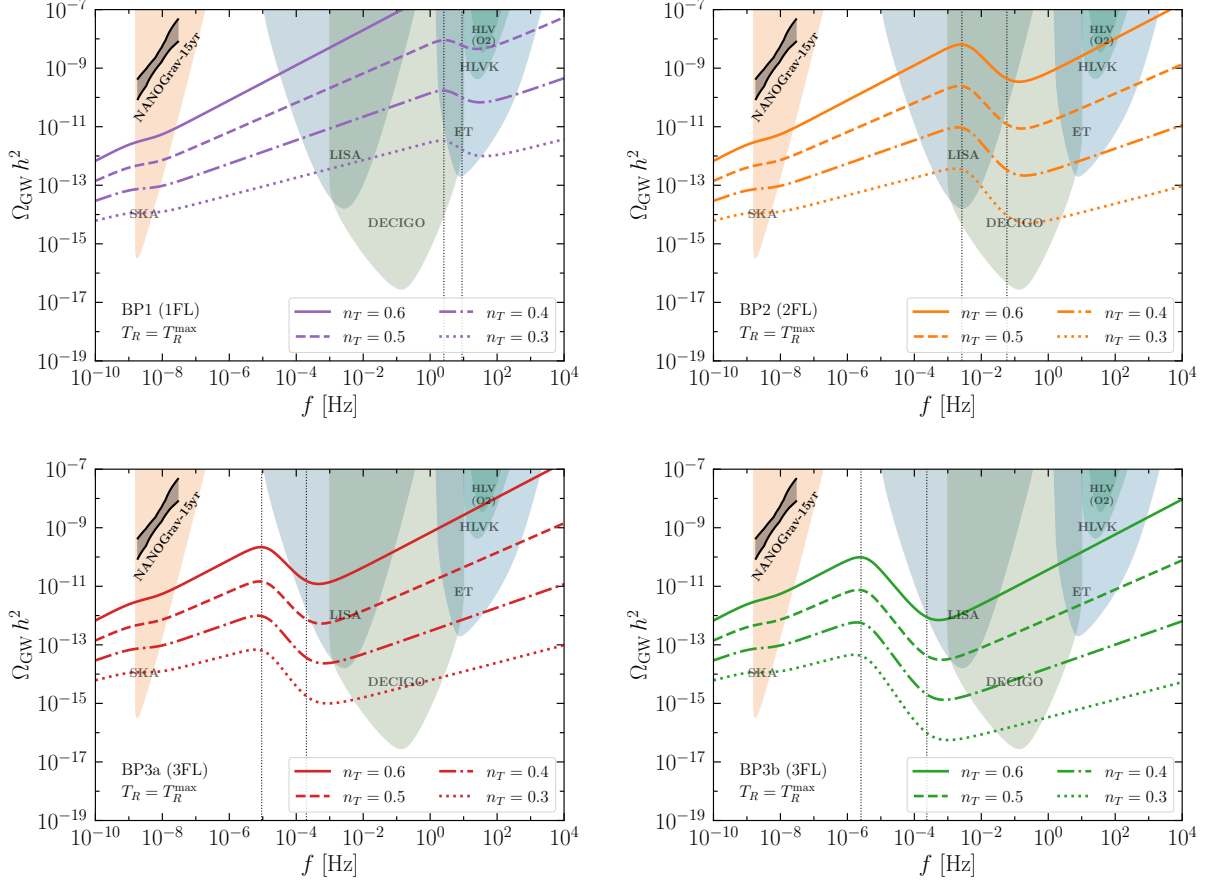


FIG. 5. Same as Fig. 4 but assuming $T_R = T_R^{\text{max}} = 10^{15}$ GeV. For all the GW spectra, the second peak frequency $f_{\text{high}}^{\text{peak}}$ occurs at 10^7 Hz, which is beyond the displayed range.

treating n_T as a free parameter. In this case, if we are able to fit a GW signal within a certain frequency band for a particular range of n_T values, we can robustly predict the GW spectrum with distinct spectral features testable at a different frequency band. As such, as shown in Figs. 4 and 5 (BP3a, bottom-left panels), a three-flavour leptogenesis scenario can predict a testable signal in the HLVK band for $0.5 \lesssim n_T \lesssim 0.6$. Therefore, if the future HLVK run finds a stochastic GW signal aligned with our anticipation, a three-flavour leptogenesis scenario would predict a signal with the similar spectral slope in the LISA range, distinct spectral behaviour in the μHz range plus a testable blue tilted signal at the nHz frequencies. We can in fact compare this signal in the nHz band with the recent PTA data. For this, we first opt for the PTA parameterization for the $\Omega_{\text{GW}}(f)$, which reads:

$$\Omega_{\text{GW}}(f) = \Omega_{\text{yr}} \left(\frac{f}{f_{\text{yr}}} \right)^{(5-\gamma)}, \quad (\text{IV.1})$$

where $\Omega_{\text{yr}} = 2\pi^2 A^2 f_{\text{yr}}^2 / (3H_0^2)$, $f_{\text{yr}} = 1 \text{ yr}^{-1} \simeq 32 \text{ nHz}$ with A and γ being the amplitude and spectral index having best-fit values⁹ $A \sim 6.4_{-2.7}^{+4.2} \times 10^{-15}$ and $\gamma \sim 3.2 \pm 0.6$. In the PTA frequency band, the $\Omega_{\text{GW}}(f)$ in Eq. (III.8) is basically $\Omega_{\text{GW}}(f) \propto f^{n_T}$, because in this range, $T_1(\xi)$ dominates,

⁹ Here we quote the NANOGrav best-fit values. Nonetheless, recently reported global posteriors [111] that include results from all the PTAs are similar to NANOGrav, because NANOGrav offers more statistically significant data among all the PTAs.

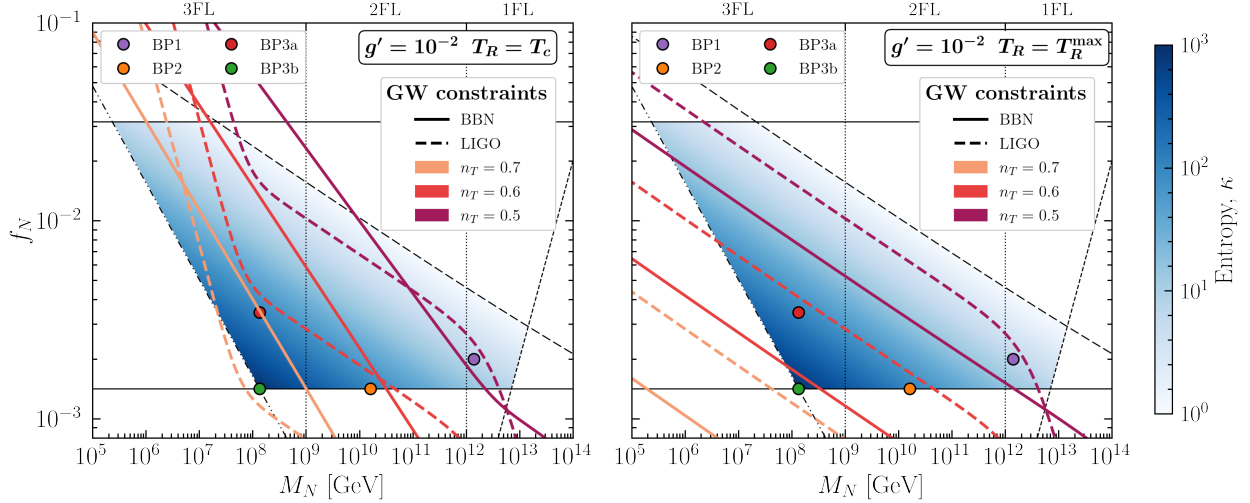


FIG. 6. BBN (solid) and LIGO (dashed) constraints on the M_N - f_N plane for different values of the tensor spectral index n_T in case of $T_R = T_c$ (left panel) and $T_R = T_R^{\max}$ (right panel). Anything to the right of these lines is excluded. Note that the constraints (especially the BBN one) depend on the reheating temperature T_R , implying that a viable tomography of flavoured leptogenesis with BGWs can be done only for $n_T \lesssim 0.7$.

and we can approximate $j_1(k\tau_0) \simeq 1/k\tau_0$. As a result, the power spectrum $P_T(k)$ in Eq. (III.6) determines the overall spectral shape. We can therefore compare Eq. (IV.1) and Eq. (III.8) to extract A and γ . For example, BP3a ($n_T = 0.6$) would provide $A \simeq 1.2 \times 10^{-16}$ and $\gamma \simeq 5 - n_T = 4.4$. Although the spectral index can be reconciled with the PTAs at 3σ CL, the amplitude is off by an order of magnitude. Remarkably, in the PTA band, this signal however mimics the one expected from GW-driven SMBHB models [112] which predict $\gamma = 13/3$ and with A^{SMBHB} in the 10^{-16} ballpark. As discussed, with our BP3a a fit to an observation of SGWB by HLVK would imply a robustly testable signal in the nHz range with $A \sim A^{\text{SMBHB}}$. Therefore, if the recent PTA finding persists, then future non-observation of nHz GWs with $A \sim A^{\text{SMBHB}}$ would imply that BP3a (or, more generally, a part of our model parameter space) would be ruled out. Notice that, the GW spectrum around the spectral index $n_T \simeq 0.6$ is the strongest and perhaps the most promising signal that the discussed flavoured leptogenesis scenario offers. This is because, in this ballpark, GWs, apart from having amplitudes $A \sim A^{\text{SMBHB}}$ at nHz and $A \sim A^{\text{HLVK}}$ at Hz, exhibit prominent and testable spectral features in the μHz and mHz bands. A higher value of n_T saturates LIGO and BBN bounds as shown in Fig. 6 (this is the reason that our scenario never produces a signal with $A \sim A^{\text{PTAs}}$). On the contrary, for $n_T \ll 0.6$, although the overall signal strength decreases and the spectrum in the nHz range loses testability, at higher frequencies the model can still provide signals with reasonably high SNR for spectral index as low as $n_T \simeq 0.3$. Below we discuss this by performing a rigorous parameter space scan of the model and taking into account all the constraints that the model has to comply with.

In Fig. 7, we report our SNR computation according to Eq. (III.22) in order to quantify the detectability of the GW signal with $n_T = 0.4$ (upper panels) and $n_T = 0.3$ (lower panels), which evade all the present constraints. In each row, the three plots from left to right correspond to the future experiments LISA, DECIGO and ET, respectively. In each plot, the thin black lines delimit the allowed parameter space in the plane according to the model constraints previously discussed. Notice that the model parameters M_N and f_N uniquely determine the spectral features of the GW signal characterized by the low peak frequency $f_{\text{low}}^{\text{peak}}$ and the dip frequency f^{dip} . Remarkably, as can be seen from the plots, the different ranges for M_N related to the different flavour regimes of

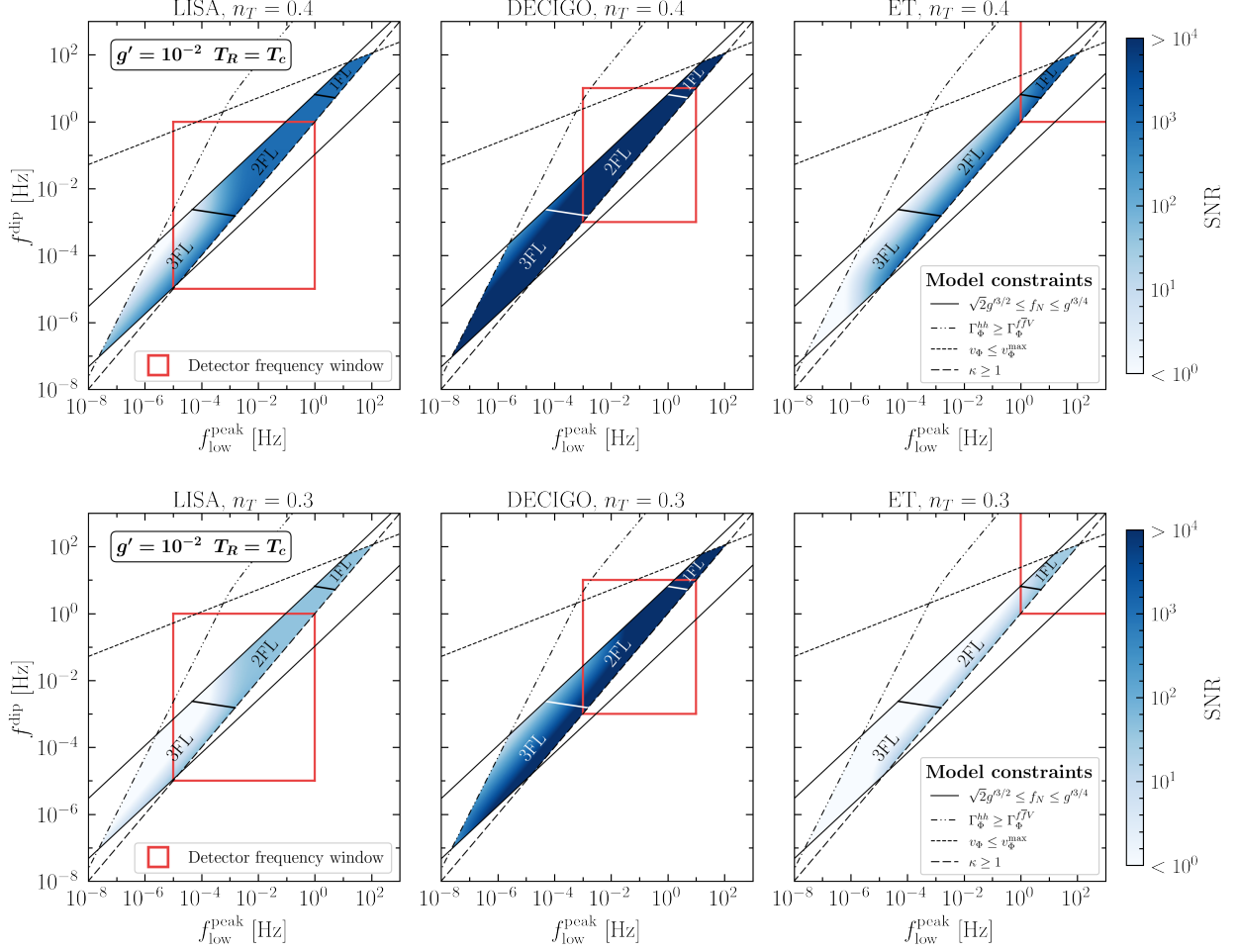


FIG. 7. Signal-to-noise ratio (SNR) with 1-year observing time (see Eq. (III.22)) for LISA, DECIGO and ET detectors in case of a GW signal with $n_T = 0.4$ (upper panels) and $n_T = 0.3$ (lower panels) in the $f_{\text{low}}^{\text{peak}}-f_{\text{dip}}$ plane. The two frequencies are uniquely determined by the model parameters M_N and f_N , and they are bounded by the thin black lines defined by several model requirements (see also Fig. 3). The red squares highlight the frequency sensitivity windows of each detector, which can be compared with the regions of the parameter space achieving three-flavour (3FL), two-flavour (2FL) and one-flavour (1FL) leptogenesis. The detectors will observe the GW spectral distortions induced by the model parameters inside the red squares.

leptogenesis are separated with 3FL, 2FL and 1FL predicting frequencies in the nHz- μ Hz, sub-Hz and Hz ranges, respectively. This further confirms that the spectral features of the GW signals trace the leptogenesis flavour regimes. We find that all the three GW detectors will potentially observe a GW signal with $n_T \gtrsim 0.3$ having $\text{SNR} \geq 1$ in most of the parameter space, while we check that DECIGO can probe GW signals with $n_T \gtrsim 0.1$. The ET detector and partially the LISA one show a smaller sensitivity to the 3FL parameter space. This trend is indeed expected since the 3FL parameters cause a distortion of the GW signal at sub- μ Hz frequencies and, consequently, lower the GW amplitude at higher frequencies hampering the detection. We stress that, in general, the SNR does not carry any spectral information being dependent on the integrated signal (see Eq. (III.22)) within the detector frequency intervals, which are highlighted with red squares in the plots. However, inside the red squares, the detectors would actually observe the spectral distortions ($f_{\text{low}}^{\text{peak}}$ as well as f_{dip}) and not just a GW power-law signal. Therefore, we find that LISA, DECIGO and ET detectors will robustly probe the three-flavour (3FL), two-flavour (2FL) and one-flavour

(1FL) regimes of leptogenesis, respectively. We emphasize that our results are not considerably affected by the choice of the reheating temperature, which is assumed to be $T_R = T_c$ in Fig. 7. On the contrary, the higher the reheating temperature, the higher the GW amplitude at frequencies higher than Hz, thus increasing the SNR at the ET detector while leaving unchanged the SNR at the LISA and DECIGO detectors.

The following concluding remarks are in order. First, a generic feature of $\Omega_{\text{GW}} \propto f^{n_T \gg 0}$ is that the spectrum does not span a wide range of frequencies due to the BBN bound on effective neutrino species. Therefore, cosmologically viable inflationary BGWs require a low reheating temperature after inflation. This has been discussed in detail in the literature and recently in the context of PTA results [16]. However, when an intermediate matter-dominated epoch is at play, the spectrum may span a wide range of frequencies without violating any cosmological bounds because of the entropy injection. It allows a high T_R , which is notably, also a natural requirement for high-scale thermal leptogenesis, as we discuss here. Therefore, high-scale leptogenesis scenarios are ideal to be searched for with BGW-spectroscopy. Let us also stress that our results depend on the parameterization of the primordial power spectrum in Eq. (III.6) and the constant value of n_T . A detailed study with a different parameterization [103, 113–115] plus considering a running of n_T [95, 96] which might induce a possible degeneracy in the predicted GW signals, is beyond the scope of this article. Second, since the last couple of years, there has been an effort to test leptogenesis with primordial GWs, see, e.g., Refs. [84, 116–128]. This article, nonetheless, for the first time, attempts to probe flavour regimes of leptogenesis with GWs. Finally, because we consider a $U(1)$ gauge symmetry breaking, our scenario must produce cosmic strings [129], which is another source of GWs [130]. We nonetheless note that we work with unconventional parameter space, which in the numerical simulations of the cosmic strings evolution are taken as $g' \sim \mathcal{O}(1)$ and $\lambda \sim \mathcal{O}(1)$ [131, 132]. A semi-analytical description covering this topic can be found in Ref.[133] which assumes that the standard computation of GW spectrum from cosmic strings holds for smaller values of g' and λ . In this article, we restrict the GW signal's detectability at the SNR level. In a follow-up publication we shall present a more precise statistical analysis to properly quantify the level of uncertainties in the reconstruction of leptogenesis parameters by means of a Fisher matrix analysis and a Markov Chain Monte Carlo estimation [134–137].

V. SUMMARY

In the present paper, for the first time, we show that flavour regimes of thermal leptogenesis can be markedly tested with gravitational waves' spectral features. Flavour effects bridge high-scale leptogenesis and low-energy neutrino physics and are important in leptogenesis computation. We opt for a tomographic method, where gravitational waves originating from an independent source, confront the leptogenesis model during their propagation in the early universe and carry imprints of leptogenesis parameters on the final gravitational waves spectrum. There are three distinct regimes of flavoured leptogenesis characterized by the right-handed neutrino mass scale: $M_N \gtrsim 10^{12}$ GeV (one-flavour/vanilla), 10^9 GeV $\lesssim M_N \lesssim 10^{12}$ GeV (two-flavour), and $M_N \lesssim 10^9$ GeV (three-flavour). Testing flavour regimes with gravitational waves is thus equivalent to studying detectable spectral features in the gravitational waves dependent on the mass scale M_N . This is possible in the simplest and well-motivated realizations of seesaw scenarios that facilitate a scalar field to give mass to the right-handed neutrinos. Apart from generating right-handed neutrino masses, the scalar field can be long-lived to provide a matter-dominated epoch with a lifetime depending on M_N . When gravitational waves pass through such a matter-dominated phase, the start, the end, and the duration of the matter-domination get imprinted on the final gravitational waves spectrum. Thus in our case, the spectral features in the GWs become dependent on M_N , hence on different regimes

of leptogenesis. While any gravitational waves that originate prior to the scalar field domination can offer a viable tomography, here we consider inflationary blue gravitational waves, which are now being widely discussed after the recent finding of blue stochastic gravitational waves by the Pulsar Timing Arrays, with an infra-red tail characterized by a simple power-law $\Omega_{\text{GW}} \sim f^{n_T}$. We show that owing to the scalar field domination, the final gravitational waves exhibit a double peak spectrum, with the characteristic frequencies (the low-frequency peak and the dip between two peaks) depending on M_N . As the leptogenesis process enters deep into the flavour regimes, the spectral features in the gravitational waves become more prominent, and the characteristic frequencies shift to lower values (see Figs 4 and 5). As such, for a two-flavour (three-flavour) regime, the low-frequency peak shows up in the mHz (μ Hz) bands. While the BBN constraint on the effective number of neutrino species and LIGO bound on stochastic gravitational waves background restrict the spectral index value $n_T \lesssim 0.7$ (see Fig. 6), a three-flavour leptogenesis scenario offers the most promising signal for $n_T \sim 0.5 - 0.6$. Indeed, it shows an amplitude testable in the next LIGO run at $f \sim \text{Hz}$, characteristic spectral features in the mHz and μ Hz bands, plus a refutable gravitational wave strain at $f \sim \text{nHz}$, comparable to the one expected from supermassive black holes. Even in case of a smaller tensor spectral index, future detectors such as LISA, DECIGO and ET will be able to probe the spectral distortions connected to the scale M_N of leptogenesis and therefore will provide remarkable insight into the leptogenesis flavour regimes (see Fig. 7).

ACKNOWLEDGEMENTS

The work of MC, RS and NS is supported by the research project TAsP (Theoretical Astroparticle Physics) funded by the Istituto Nazionale di Fisica Nucleare (INFN). The work of NS is further supported by the research grant number 2022E2J4RK ‘‘PANTHEON: Perspectives in Astroparticle and Neutrino THEory with Old and New messengers’’ under the program PRIN 2022 funded by the Italian Ministero dell’Universit a e della Ricerca (MUR). The work of SD is supported by the National Natural Science Foundation of China (NNSFC) under grant No. 12150610460.

Appendix A: Varying the $B - L$ gauge coupling

Similar to Fig. 6 ($g' = 10^{-2}$), to show the qualitative trend and dependence on gauge coupling, we present the allowed parameter space for $g' = 0.05$ and 10^{-3} in Figs 8 and 9, respectively. Note that larger values of gauge coupling result in a shrinking of the parameter space because of the imposed constraints and lesser entropy production (cf. Eq. (II.7), Eq. (II.8), and Eq. (II.13)). As discussed in the main text, the smaller the entropy production, the less the suppression in GWs. Therefore, compared to the $g' = 10^{-2}$ case, smaller values of the spectral indices are now allowed by the LIGO and the BBN. On the contrary, for smaller values of g' , the allowed parameter space enlarges plus the LIGO and the BBN limits allow for larger values of the spectral indices. Note in either case, the qualitative features in the GW spectrum, however, remain intact. For example, for a 3FL we would get the low-frequency peak at smaller frequencies than a 2FL. Compared to the $g' = 10^{-2}$ case, however, this peak would shift to the right (left) for larger (smaller) values of gauge couplings (cf. Fig. 4).

[1] A. H. Guth, The Inflationary Universe: A Possible Solution to the Horizon and Flatness Problems, *Phys. Rev. D* **23**, 347 (1981).

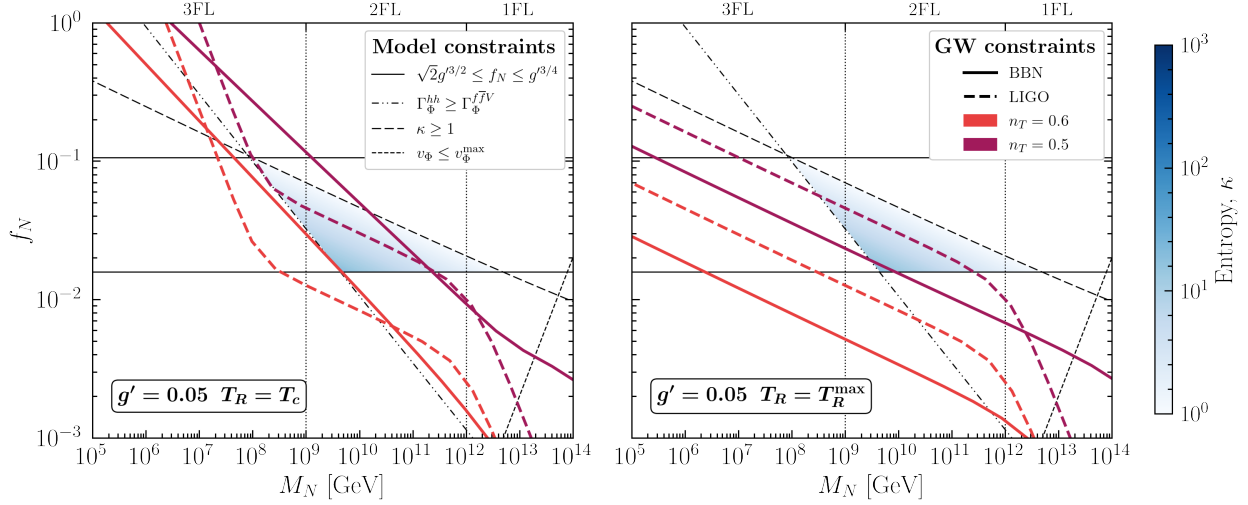


FIG. 8. Allowed parameter space with $g' = 0.05$ for $T_R = T_c$ (left panel) and $T_R = T_R^{\max}$ (right panel). The texture and the color codes for all the curves representing the constraints are the same as in Fig.6. Note that, compared to the $g' = 10^{-2}$ case, smaller values of spectral indices are required because of less entropy production.

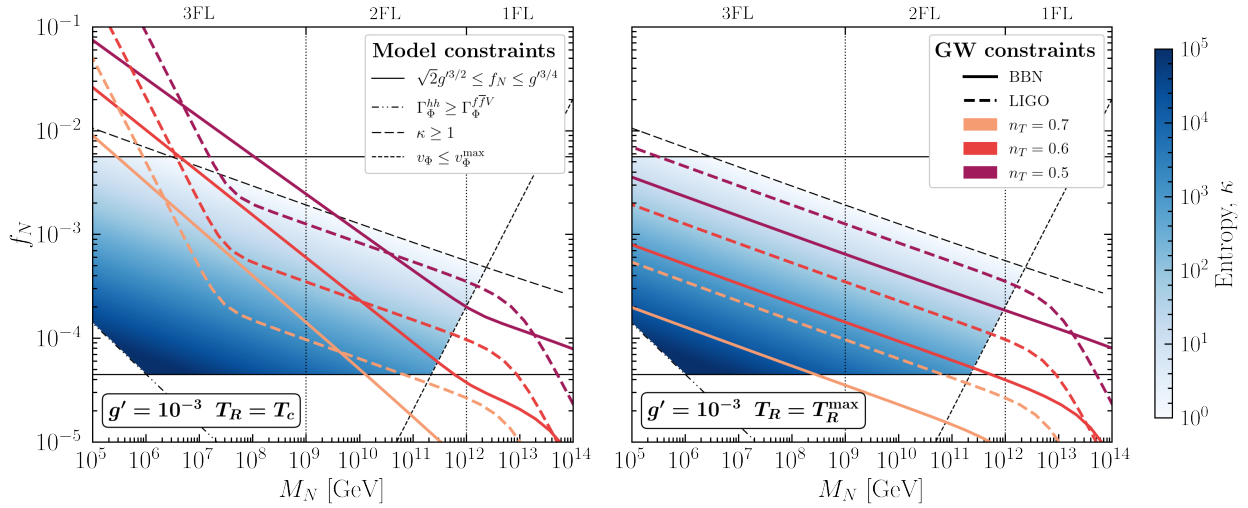


FIG. 9. Allowed parameter space with $g' = 10^{-3}$ for $T_R = T_c$ (left panel) and $T_R = T_R^{\max}$ (right panel). The texture and the color codes for all the curves representing the constraints are the same as in Fig.6. Note that, compared to the $g' = 10^{-2}$ case, larger values of spectral indices are allowed because of larger entropy production.

- [2] A. D. Linde, A New Inflationary Universe Scenario: A Possible Solution of the Horizon, Flatness, Homogeneity, Isotropy and Primordial Monopole Problems, *Phys. Lett. B* **108**, 389 (1982).
- [3] S. Datta and R. Samanta, Gravitational waves-tomography of Low-Scale-Leptogenesis, *JHEP* **11**, 159, [arXiv:2208.09949 \[hep-ph\]](#).
- [4] S. Datta and R. Samanta, Fingerprints of GeV scale right-handed neutrinos on inflationary gravitational waves and PTA data, *Phys. Rev. D* **108**, L091706 (2023), [arXiv:2307.00646 \[hep-ph\]](#).
- [5] M. Fukugita and T. Yanagida, Baryogenesis Without Grand Unification, *Phys. Lett. B* **174**, 45 (1986).
- [6] G. Agazie *et al.* (NANOGrav), The NANOGrav 15 yr Data Set: Evidence for a Gravitational-wave Background, *Astrophys. J. Lett.* **951**, L8 (2023), [arXiv:2306.16213 \[astro-ph.HE\]](#).

- [7] J. Antoniadis *et al.* (EPTA, InPTA:), The second data release from the European Pulsar Timing Array - III. Search for gravitational wave signals, *Astron. Astrophys.* **678**, A50 (2023), [arXiv:2306.16214 \[astro-ph.HE\]](#).
- [8] D. J. Reardon *et al.*, Search for an Isotropic Gravitational-wave Background with the Parkes Pulsar Timing Array, *Astrophys. J. Lett.* **951**, L6 (2023), [arXiv:2306.16215 \[astro-ph.HE\]](#).
- [9] H. Xu *et al.*, Searching for the Nano-Hertz Stochastic Gravitational Wave Background with the Chinese Pulsar Timing Array Data Release I, *Res. Astron. Astrophys.* **23**, 075024 (2023), [arXiv:2306.16216 \[astro-ph.HE\]](#).
- [10] A. Afzal *et al.* (NANOGrav), The NANOGrav 15 yr Data Set: Search for Signals from New Physics, *Astrophys. J. Lett.* **951**, L11 (2023), [arXiv:2306.16219 \[astro-ph.HE\]](#).
- [11] J. Antoniadis *et al.* (EPTA, InPTA), The second data release from the European Pulsar Timing Array - IV. Implications for massive black holes, dark matter, and the early Universe, *Astron. Astrophys.* **685**, A94 (2024), [arXiv:2306.16227 \[astro-ph.CO\]](#).
- [12] S. Vagnozzi, Implications of the NANOGrav results for inflation, *Mon. Not. Roy. Astron. Soc.* **502**, L11 (2021), [arXiv:2009.13432 \[astro-ph.CO\]](#).
- [13] S. Bhattacharya, S. Mohanty, and P. Parashari, Implications of the NANOGrav result on primordial gravitational waves in nonstandard cosmologies, *Phys. Rev. D* **103**, 063532 (2021), [arXiv:2010.05071 \[astro-ph.CO\]](#).
- [14] S. Kuroyanagi, T. Takahashi, and S. Yokoyama, Blue-tilted inflationary tensor spectrum and reheating in the light of NANOGrav results, *JCAP* **01**, 071, [arXiv:2011.03323 \[astro-ph.CO\]](#).
- [15] M. Benetti, L. L. Graef, and S. Vagnozzi, Primordial gravitational waves from NANOGrav: A broken power-law approach, *Phys. Rev. D* **105**, 043520 (2022), [arXiv:2111.04758 \[astro-ph.CO\]](#).
- [16] S. Vagnozzi, Inflationary interpretation of the stochastic gravitational wave background signal detected by pulsar timing array experiments, *JHEAp* **39**, 81 (2023), [arXiv:2306.16912 \[astro-ph.CO\]](#).
- [17] D. Borah, S. Jyoti Das, and R. Samanta, Imprint of inflationary gravitational waves and WIMP dark matter in pulsar timing array data, *JCAP* **03**, 031, [arXiv:2307.00537 \[hep-ph\]](#).
- [18] W. DeRocco and J. A. Dror, Using Pulsar Parameter Drifts to Detect Subnanohertz Gravitational Waves, *Phys. Rev. Lett.* **132**, 101403 (2024), [arXiv:2212.09751 \[astro-ph.HE\]](#).
- [19] W. DeRocco and J. A. Dror, Searching for stochastic gravitational waves below a nanohertz, *Phys. Rev. D* **108**, 103011 (2023), [arXiv:2304.13042 \[astro-ph.HE\]](#).
- [20] D. Blas and A. C. Jenkins, Bridging the μHz Gap in the Gravitational-Wave Landscape with Binary Resonances, *Phys. Rev. Lett.* **128**, 101103 (2022), [arXiv:2107.04601 \[astro-ph.CO\]](#).
- [21] D. Blas and A. C. Jenkins, Detecting stochastic gravitational waves with binary resonance, *Phys. Rev. D* **105**, 064021 (2022), [arXiv:2107.04063 \[gr-qc\]](#).
- [22] P. Bari, A. Ricciardone, N. Bartolo, D. Bertacca, and S. Matarrese, Signatures of Primordial Gravitational Waves on the Large-Scale Structure of the Universe, *Phys. Rev. Lett.* **129**, 091301 (2022), [arXiv:2111.06884 \[astro-ph.CO\]](#).
- [23] A. Gruzinov, Elastic inflation, *Phys. Rev. D* **70**, 063518 (2004), [arXiv:astro-ph/0404548](#).
- [24] T. Kobayashi, M. Yamaguchi, and J. Yokoyama, G-inflation: Inflation driven by the Galileon field, *Phys. Rev. Lett.* **105**, 231302 (2010), [arXiv:1008.0603 \[hep-th\]](#).
- [25] S. Endlich, A. Nicolis, and J. Wang, Solid Inflation, *JCAP* **10**, 011, [arXiv:1210.0569 \[hep-th\]](#).
- [26] D. Cannone, G. Tasinato, and D. Wands, Generalised tensor fluctuations and inflation, *JCAP* **01**, 029, [arXiv:1409.6568 \[astro-ph.CO\]](#).
- [27] A. Ricciardone and G. Tasinato, Primordial gravitational waves in supersolid inflation, *Phys. Rev. D* **96**, 023508 (2017), [arXiv:1611.04516 \[astro-ph.CO\]](#).
- [28] Y.-F. Cai, J.-O. Gong, S. Pi, E. N. Saridakis, and S.-Y. Wu, On the possibility of blue tensor spectrum within single field inflation, *Nucl. Phys. B* **900**, 517 (2015), [arXiv:1412.7241 \[hep-th\]](#).
- [29] T. Fujita, S. Kuroyanagi, S. Mizuno, and S. Mukohyama, Blue-tilted Primordial Gravitational Waves from Massive Gravity, *Phys. Lett. B* **789**, 215 (2019), [arXiv:1808.02381 \[gr-qc\]](#).
- [30] Y. Mishima and T. Kobayashi, Revisiting slow-roll dynamics and the tensor tilt in general single-field inflation, *Phys. Rev. D* **101**, 043536 (2020), [arXiv:1911.02143 \[gr-qc\]](#).
- [31] S. Pan, Y. Cai, and Y.-S. Piao, Climbing over the potential barrier during inflation via null energy condition violation, *Eur. Phys. J. C* **84**, 976 (2024), [arXiv:2404.12655 \[astro-ph.CO\]](#).
- [32] S. Datta, Explaining PTA Data with Inflationary GWs in a PBH-Dominated Universe, (2023), [arXiv:2309.14238 \[hep-ph\]](#).

- [33] A. Weltman *et al.*, Fundamental physics with the Square Kilometre Array, *Publ. Astron. Soc. Austral.* **37**, e002 (2020), [arXiv:1810.02680 \[astro-ph.CO\]](#).
- [34] J. Garcia-Bellido, H. Murayama, and G. White, Exploring the early Universe with Gaia and Theia, *JCAP* **12** (12), 023, [arXiv:2104.04778 \[hep-ph\]](#).
- [35] A. Sesana *et al.*, Unveiling the gravitational universe at μ -Hz frequencies, *Exper. Astron.* **51**, 1333 (2021), [arXiv:1908.11391 \[astro-ph.IM\]](#).
- [36] P. Amaro-Seoane *et al.* (LISA), Laser Interferometer Space Antenna, (2017), [arXiv:1702.00786 \[astro-ph.IM\]](#).
- [37] J. Baker *et al.*, The Laser Interferometer Space Antenna: Unveiling the Millihertz Gravitational Wave Sky, (2019), [arXiv:1907.06482 \[astro-ph.IM\]](#).
- [38] K. Yagi and N. Seto, Detector configuration of DECIGO/BBO and identification of cosmological neutron-star binaries, *Phys. Rev. D* **83**, 044011 (2011), [Erratum: *Phys.Rev.D* 95, 109901 (2017)], [arXiv:1101.3940 \[astro-ph.CO\]](#).
- [39] S. Kawamura *et al.*, The Japanese space gravitational wave antenna DECIGO, *Class. Quant. Grav.* **23**, S125 (2006).
- [40] S. Isoyama, H. Nakano, and T. Nakamura, Multiband Gravitational-Wave Astronomy: Observing binary inspirals with a decihertz detector, B-DECIGO, *PTEP* **2018**, 073E01 (2018), [arXiv:1802.06977 \[gr-qc\]](#).
- [41] B. Sathyaprakash *et al.*, Scientific Objectives of Einstein Telescope, *Class. Quant. Grav.* **29**, 124013 (2012), [Erratum: *Class.Quant.Grav.* 30, 079501 (2013)], [arXiv:1206.0331 \[gr-qc\]](#).
- [42] M. Maggiore *et al.*, Science Case for the Einstein Telescope, *JCAP* **03**, 050, [arXiv:1912.02622 \[astro-ph.CO\]](#).
- [43] B. P. Abbott *et al.* (LIGO Scientific), Exploring the Sensitivity of Next Generation Gravitational Wave Detectors, *Class. Quant. Grav.* **34**, 044001 (2017), [arXiv:1607.08697 \[astro-ph.IM\]](#).
- [44] R. Abbott *et al.* (KAGRA, Virgo, LIGO Scientific), Upper limits on the isotropic gravitational-wave background from Advanced LIGO and Advanced Virgo's third observing run, *Phys. Rev. D* **104**, 022004 (2021), [arXiv:2101.12130 \[gr-qc\]](#).
- [45] B. P. Abbott *et al.* (LIGO Scientific, Virgo), A guide to LIGO–Virgo detector noise and extraction of transient gravitational-wave signals, *Class. Quant. Grav.* **37**, 055002 (2020), [arXiv:1908.11170 \[gr-qc\]](#).
- [46] V. A. Kuzmin, V. A. Rubakov, and M. E. Shaposhnikov, On the Anomalous Electroweak Baryon Number Nonconservation in the Early Universe, *Phys. Lett. B* **155**, 36 (1985).
- [47] L. Alvarez-Gaume and E. Witten, Gravitational Anomalies, *Nucl. Phys. B* **234**, 269 (1984).
- [48] S. H.-S. Alexander, M. E. Peskin, and M. M. Sheikh-Jabbari, Leptogenesis from gravity waves in models of inflation, *Phys. Rev. Lett.* **96**, 081301 (2006), [arXiv:hep-th/0403069](#).
- [49] A. G. Cohen and D. B. Kaplan, Thermodynamic Generation of the Baryon Asymmetry, *Phys. Lett. B* **199**, 251 (1987).
- [50] A. Riotto and M. Trodden, Recent progress in baryogenesis, *Ann. Rev. Nucl. Part. Sci.* **49**, 35 (1999), [arXiv:hep-ph/9901362](#).
- [51] A. Pilaftsis and T. E. J. Underwood, Resonant leptogenesis, *Nucl. Phys. B* **692**, 303 (2004), [arXiv:hep-ph/0309342](#).
- [52] W. Buchmuller, P. Di Bari, and M. Plumacher, Leptogenesis for pedestrians, *Annals Phys.* **315**, 305 (2005), [arXiv:hep-ph/0401240](#).
- [53] S. Davidson, E. Nardi, and Y. Nir, Leptogenesis, *Phys. Rept.* **466**, 105 (2008), [arXiv:0802.2962 \[hep-ph\]](#).
- [54] D. Bodeker and W. Buchmuller, Baryogenesis from the weak scale to the grand unification scale, *Rev. Mod. Phys.* **93**, 035004 (2021), [arXiv:2009.07294 \[hep-ph\]](#).
- [55] P. Di Bari, On the origin of matter in the Universe, *Prog. Part. Nucl. Phys.* **122**, 103913 (2022), [arXiv:2107.13750 \[hep-ph\]](#).
- [56] S. Davidson and A. Ibarra, A Lower bound on the right-handed neutrino mass from leptogenesis, *Phys. Lett. B* **535**, 25 (2002), [arXiv:hep-ph/0202239](#).
- [57] E. K. Akhmedov, V. A. Rubakov, and A. Y. Smirnov, Baryogenesis via neutrino oscillations, *Phys. Rev. Lett.* **81**, 1359 (1998), [arXiv:hep-ph/9803255](#).
- [58] T. Hambye and D. Teresi, Higgs doublet decay as the origin of the baryon asymmetry, *Phys. Rev. Lett.* **117**, 091801 (2016), [arXiv:1606.00017 \[hep-ph\]](#).

- [59] P. S. Bhupal Dev, P. Millington, A. Pilaftsis, and D. Teresi, Flavour Covariant Transport Equations: an Application to Resonant Leptogenesis, *Nucl. Phys. B* **886**, 569 (2014), [arXiv:1404.1003 \[hep-ph\]](#).
- [60] A. Abada, S. Davidson, A. Ibarra, F. X. Josse-Michaux, M. Losada, and A. Riotto, Flavour Matters in Leptogenesis, *JHEP* **09**, 010, [arXiv:hep-ph/0605281](#).
- [61] E. Nardi, Y. Nir, E. Roulet, and J. Racker, The Importance of flavor in leptogenesis, *JHEP* **01**, 164, [arXiv:hep-ph/0601084](#).
- [62] S. Blanchet and P. Di Bari, Flavor effects on leptogenesis predictions, *JCAP* **03**, 018, [arXiv:hep-ph/0607330](#).
- [63] S. Pascoli, S. T. Petcov, and A. Riotto, Leptogenesis and Low Energy CP Violation in Neutrino Physics, *Nucl. Phys. B* **774**, 1 (2007), [arXiv:hep-ph/0611338](#).
- [64] G. Altarelli and F. Feruglio, Discrete Flavor Symmetries and Models of Neutrino Mixing, *Rev. Mod. Phys.* **82**, 2701 (2010), [arXiv:1002.0211 \[hep-ph\]](#).
- [65] S. F. King, Unified Models of Neutrinos, Flavour and CP Violation, *Prog. Part. Nucl. Phys.* **94**, 217 (2017), [arXiv:1701.04413 \[hep-ph\]](#).
- [66] A. Davidson, $B - L$ as the fourth color within an $SU(2)_L \times U(1)_R \times U(1)$ model, *Phys. Rev. D* **20**, 776 (1979).
- [67] R. E. Marshak and R. N. Mohapatra, Quark - Lepton Symmetry and B-L as the U(1) Generator of the Electroweak Symmetry Group, *Phys. Lett. B* **91**, 222 (1980).
- [68] R. N. Mohapatra and R. E. Marshak, Local B-L Symmetry of Electroweak Interactions, Majorana Neutrinos and Neutron Oscillations, *Phys. Rev. Lett.* **44**, 1316 (1980), [Erratum: *Phys.Rev.Lett.* 44, 1643 (1980)].
- [69] W. Buchmüller, V. Domcke, K. Kamada, and K. Schmitz, The Gravitational Wave Spectrum from Cosmological $B - L$ Breaking, *JCAP* **10**, 003, [arXiv:1305.3392 \[hep-ph\]](#).
- [70] W. Buchmuller, V. Domcke, H. Murayama, and K. Schmitz, Probing the scale of grand unification with gravitational waves, *Phys. Lett. B* **809**, 135764 (2020), [arXiv:1912.03695 \[hep-ph\]](#).
- [71] P. Minkowski, $\mu \rightarrow e\gamma$ at a Rate of One Out of 10^9 Muon Decays?, *Phys. Lett. B* **67**, 421 (1977).
- [72] M. Gell-Mann, P. Ramond, and R. Slansky, Complex Spinors and Unified Theories, *Conf. Proc. C* **790927**, 315 (1979), [arXiv:1306.4669 \[hep-th\]](#).
- [73] T. Yanagida, Horizontal Symmetry and Masses of Neutrinos, *Prog. Theor. Phys.* **64**, 1103 (1980).
- [74] R. N. Mohapatra, Mechanism for Understanding Small Neutrino Mass in Superstring Theories, *Phys. Rev. Lett.* **56**, 561 (1986).
- [75] A. D. Linde, Phase Transitions in Gauge Theories and Cosmology, *Rept. Prog. Phys.* **42**, 389 (1979).
- [76] T. W. B. Kibble, Some Implications of a Cosmological Phase Transition, *Phys. Rept.* **67**, 183 (1980).
- [77] M. Quiros, Finite temperature field theory and phase transitions, in *ICTP Summer School in High-Energy Physics and Cosmology* (1999) pp. 187–259, [arXiv:hep-ph/9901312](#).
- [78] C. Caprini *et al.*, Science with the space-based interferometer eLISA. II: Gravitational waves from cosmological phase transitions, *JCAP* **04**, 001, [arXiv:1512.06239 \[astro-ph.CO\]](#).
- [79] M. B. Hindmarsh, M. Lüben, J. Lumma, and M. Pauly, Phase transitions in the early universe, *SciPost Phys. Lect. Notes* **24**, 1 (2021), [arXiv:2008.09136 \[astro-ph.CO\]](#).
- [80] A. Megevand and S. Ramirez, Bubble nucleation and growth in very strong cosmological phase transitions, *Nucl. Phys. B* **919**, 74 (2017), [arXiv:1611.05853 \[astro-ph.CO\]](#).
- [81] C. Gross, O. Lebedev, and M. Zatta, Higgs-inflaton coupling from reheating and the metastable Universe, *Phys. Lett. B* **753**, 178 (2016), [arXiv:1506.05106 \[hep-ph\]](#).
- [82] K. Enqvist, M. Karčiauskas, O. Lebedev, S. Rusak, and M. Zatta, Postinflationary vacuum instability and Higgs-inflaton couplings, *JCAP* **11**, 025, [arXiv:1608.08848 \[hep-ph\]](#).
- [83] D. Croon, N. Fernandez, D. McKeen, and G. White, Stability, reheating and leptogenesis, *JHEP* **06**, 098, [arXiv:1903.08658 \[hep-ph\]](#).
- [84] S. Blasi, V. Brdar, and K. Schmitz, Fingerprint of low-scale leptogenesis in the primordial gravitational-wave spectrum, *Phys. Rev. Res.* **2**, 043321 (2020), [arXiv:2004.02889 \[hep-ph\]](#).
- [85] P. A. R. Ade *et al.* (Planck), Planck 2015 results. XIII. Cosmological parameters, *Astron. Astrophys.* **594**, A13 (2016), [arXiv:1502.01589 \[astro-ph.CO\]](#).
- [86] T. Han and X. Wang, Radiative Decays of the Higgs Boson to a Pair of Fermions, *JHEP* **10**, 036, [arXiv:1704.00790 \[hep-ph\]](#).
- [87] B. Holdom, Two U(1)'s and Epsilon Charge Shifts, *Phys. Lett. B* **166**, 196 (1986).

- [88] C. Cheung, J. T. Ruderman, L.-T. Wang, and I. Yavin, Kinetic Mixing as the Origin of Light Dark Scales, *Phys. Rev. D* **80**, 035008 (2009), [arXiv:0902.3246 \[hep-ph\]](#).
- [89] T. Gherghetta, J. Kersten, K. Olive, and M. Pospelov, Evaluating the price of tiny kinetic mixing, *Phys. Rev. D* **100**, 095001 (2019), [arXiv:1909.00696 \[hep-ph\]](#).
- [90] A. Hook, E. Izaguirre, and J. G. Wacker, Model Independent Bounds on Kinetic Mixing, *Adv. High Energy Phys.* **2011**, 859762 (2011), [arXiv:1006.0973 \[hep-ph\]](#).
- [91] S. Weinberg, Damping of tensor modes in cosmology, *Phys. Rev. D* **69**, 023503 (2004), [arXiv:astro-ph/0306304](#).
- [92] W. Zhao, Y. Zhang, and T. Xia, New method to constrain the relativistic free-streaming gas in the Universe, *Phys. Lett. B* **677**, 235 (2009), [arXiv:0905.3223 \[astro-ph.CO\]](#).
- [93] L. Page *et al.* (WMAP), Three year Wilkinson Microwave Anisotropy Probe (WMAP) observations: polarization analysis, *Astrophys. J. Suppl.* **170**, 335 (2007), [arXiv:astro-ph/0603450](#).
- [94] P. A. R. Ade *et al.* (BICEP2, Keck Array), BICEP2 / Keck Array x: Constraints on Primordial Gravitational Waves using Planck, WMAP, and New BICEP2/Keck Observations through the 2015 Season, *Phys. Rev. Lett.* **121**, 221301 (2018), [arXiv:1810.05216 \[astro-ph.CO\]](#).
- [95] S. Kuroyanagi and T. Takahashi, Higher Order Corrections to the Primordial Gravitational Wave Spectrum and its Impact on Parameter Estimates for Inflation, *JCAP* **10**, 006, [arXiv:1106.3437 \[astro-ph.CO\]](#).
- [96] G. Calcagni and S. Kuroyanagi, Stochastic gravitational-wave background in quantum gravity, *JCAP* **03**, 019, [arXiv:2012.00170 \[gr-qc\]](#).
- [97] A. R. Liddle and D. H. Lyth, The Cold dark matter density perturbation, *Phys. Rept.* **231**, 1 (1993), [arXiv:astro-ph/9303019](#).
- [98] N. Seto and J. Yokoyama, Probing the equation of state of the early universe with a space laser interferometer, *J. Phys. Soc. Jap.* **72**, 3082 (2003), [arXiv:gr-qc/0305096](#).
- [99] L. A. Boyle and P. J. Steinhardt, Probing the early universe with inflationary gravitational waves, *Phys. Rev. D* **77**, 063504 (2008), [arXiv:astro-ph/0512014](#).
- [100] K. Nakayama, S. Saito, Y. Suwa, and J. Yokoyama, Probing reheating temperature of the universe with gravitational wave background, *JCAP* **06**, 020, [arXiv:0804.1827 \[astro-ph\]](#).
- [101] S. Kuroyanagi, T. Chiba, and N. Sugiyama, Precision calculations of the gravitational wave background spectrum from inflation, *Phys. Rev. D* **79**, 103501 (2009), [arXiv:0804.3249 \[astro-ph\]](#).
- [102] K. Nakayama and J. Yokoyama, Gravitational Wave Background and Non-Gaussianity as a Probe of the Curvaton Scenario, *JCAP* **01**, 010, [arXiv:0910.0715 \[astro-ph.CO\]](#).
- [103] S. Kuroyanagi, T. Takahashi, and S. Yokoyama, Blue-tilted Tensor Spectrum and Thermal History of the Universe, *JCAP* **02**, 003, [arXiv:1407.4785 \[astro-ph.CO\]](#).
- [104] Y. Watanabe and E. Komatsu, Improved Calculation of the Primordial Gravitational Wave Spectrum in the Standard Model, *Phys. Rev. D* **73**, 123515 (2006), [arXiv:astro-ph/0604176](#).
- [105] K. Saikawa and S. Shirai, Primordial gravitational waves, precisely: The role of thermodynamics in the Standard Model, *JCAP* **05**, 035, [arXiv:1803.01038 \[hep-ph\]](#).
- [106] A. Peimbert, M. Peimbert, and V. Luridiana, The primordial helium abundance and the number of neutrino families, *Rev. Mex. Astron. Astrofis.* **52**, 419 (2016), [arXiv:1608.02062 \[astro-ph.CO\]](#).
- [107] B. P. Abbott *et al.* (LIGO Scientific, Virgo), Upper Limits on the Stochastic Gravitational-Wave Background from Advanced LIGO's First Observing Run, *Phys. Rev. Lett.* **118**, 121101 (2017), [Erratum: *Phys.Rev.Lett.* 119, 029901 (2017)], [arXiv:1612.02029 \[gr-qc\]](#).
- [108] R. Abbott *et al.* (KAGRA, Virgo, LIGO Scientific), Upper limits on the isotropic gravitational-wave background from Advanced LIGO and Advanced Virgo's third observing run, *Phys. Rev. D* **104**, 022004 (2021), [arXiv:2101.12130 \[gr-qc\]](#).
- [109] M. Maggiore, Gravitational wave experiments and early universe cosmology, *Phys. Rept.* **331**, 283 (2000), [arXiv:gr-qc/9909001](#).
- [110] K. Schmitz, New Sensitivity Curves for Gravitational-Wave Signals from Cosmological Phase Transitions, *JHEP* **01**, 097, [arXiv:2002.04615 \[hep-ph\]](#).
- [111] G. Agazie *et al.* (International Pulsar Timing Array), Comparing Recent Pulsar Timing Array Results on the Nanohertz Stochastic Gravitational-wave Background, *Astrophys. J.* **966**, 105 (2024), [arXiv:2309.00693 \[astro-ph.HE\]](#).
- [112] E. S. Phinney, A Practical theorem on gravitational wave backgrounds, (2001), [arXiv:astro-ph/0108028](#).

- [113] J.-Q. Jiang, Y. Cai, G. Ye, and Y.-S. Piao, Broken blue-tilted inflationary gravitational waves: a joint analysis of NANOGrav 15-year and BICEP/Keck 2018 data, *JCAP* **05**, 004, [arXiv:2307.15547 \[astro-ph.CO\]](#).
- [114] Y. Cai and Y.-S. Piao, Intermittent null energy condition violations during inflation and primordial gravitational waves, *Phys. Rev. D* **103**, 083521 (2021), [arXiv:2012.11304 \[gr-qc\]](#).
- [115] W. Giarè, M. Forconi, E. Di Valentino, and A. Melchiorri, Towards a reliable calculation of relic radiation from primordial gravitational waves, *Mon. Not. Roy. Astron. Soc.* **520**, 2 (2023), [arXiv:2210.14159 \[astro-ph.CO\]](#).
- [116] J. A. Dror, T. Hiramatsu, K. Kohri, H. Murayama, and G. White, Testing the Seesaw Mechanism and Leptogenesis with Gravitational Waves, *Phys. Rev. Lett.* **124**, 041804 (2020), [arXiv:1908.03227 \[hep-ph\]](#).
- [117] R. Samanta and S. Datta, Gravitational wave complementarity and impact of NANOGrav data on gravitational leptogenesis, *JHEP* **05**, 211, [arXiv:2009.13452 \[hep-ph\]](#).
- [118] S. Datta, A. Ghosal, and R. Samanta, Baryogenesis from ultralight primordial black holes and strong gravitational waves from cosmic strings, *JCAP* **08**, 021, [arXiv:2012.14981 \[hep-ph\]](#).
- [119] B. Barman, D. Borah, A. Dasgupta, and A. Ghoshal, Probing high scale Dirac leptogenesis via gravitational waves from domain walls, *Phys. Rev. D* **106**, 015007 (2022), [arXiv:2205.03422 \[hep-ph\]](#).
- [120] A. Dasgupta, P. S. B. Dev, A. Ghoshal, and A. Mazumdar, Gravitational wave pathway to testable leptogenesis, *Phys. Rev. D* **106**, 075027 (2022), [arXiv:2206.07032 \[hep-ph\]](#).
- [121] D. Borah, S. Jyoti Das, R. Samanta, and F. R. Urban, PBH-infused seesaw origin of matter and unique gravitational waves, *JHEP* **03**, 127, [arXiv:2211.15726 \[hep-ph\]](#).
- [122] Y. F. Perez-Gonzalez and J. Turner, Assessing the tension between a black hole dominated early universe and leptogenesis, *Phys. Rev. D* **104**, 103021 (2021), [arXiv:2010.03565 \[hep-ph\]](#).
- [123] A. Ghoshal, R. Samanta, and G. White, Bremsstrahlung high-frequency gravitational wave signatures of high-scale nonthermal leptogenesis, *Phys. Rev. D* **108**, 035019 (2023), [arXiv:2211.10433 \[hep-ph\]](#).
- [124] P. Huang and K.-P. Xie, Leptogenesis triggered by a first-order phase transition, *JHEP* **09**, 052, [arXiv:2206.04691 \[hep-ph\]](#).
- [125] D. Borah, A. Dasgupta, and I. Saha, Leptogenesis and dark matter through relativistic bubble walls with observable gravitational waves, *JHEP* **11**, 136, [arXiv:2207.14226 \[hep-ph\]](#).
- [126] E. J. Chun, T. P. Dutka, T. H. Jung, X. Nagels, and M. Vanvlasselaer, Bubble-assisted leptogenesis, *JHEP* **09**, 164, [arXiv:2305.10759 \[hep-ph\]](#).
- [127] A. Azatov, M. Vanvlasselaer, and W. Yin, Baryogenesis via relativistic bubble walls, *JHEP* **10**, 043, [arXiv:2106.14913 \[hep-ph\]](#).
- [128] B. Barman, D. Borah, S. Das Jyoti, and R. Roshan, Cogenesis of Baryon asymmetry and gravitational dark matter from primordial black holes, *JCAP* **08**, 068, [arXiv:2204.10339 \[hep-ph\]](#).
- [129] T. W. B. Kibble, Topology of Cosmic Domains and Strings, *J. Phys. A* **9**, 1387 (1976).
- [130] A. Vilenkin, Gravitational radiation from cosmic strings, *Phys. Lett. B* **107**, 47 (1981).
- [131] J. J. Blanco-Pillado, K. D. Olum, and B. Shlaer, Large parallel cosmic string simulations: New results on loop production, *Phys. Rev. D* **83**, 083514 (2011), [arXiv:1101.5173 \[astro-ph.CO\]](#).
- [132] D. Matsunami, L. Pogosian, A. Saurabh, and T. Vachaspati, Decay of Cosmic String Loops Due to Particle Radiation, *Phys. Rev. Lett.* **122**, 201301 (2019), [arXiv:1903.05102 \[hep-ph\]](#).
- [133] M. Chianese, S. Datta, G. Miele, R. Samanta, and N. Saviano, Probing flavored regimes of leptogenesis with gravitational waves from cosmic strings, (2024), [arXiv:2406.01231 \[hep-ph\]](#).
- [134] R. Flauger, N. Karnesis, G. Nardini, M. Pieroni, A. Ricciardone, and J. Torrado, Improved reconstruction of a stochastic gravitational wave background with LISA, *JCAP* **01**, 059, [arXiv:2009.11845 \[astro-ph.CO\]](#).
- [135] C. Gowling and M. Hindmarsh, Observational prospects for phase transitions at LISA: Fisher matrix analysis, *JCAP* **10**, 039, [arXiv:2106.05984 \[astro-ph.CO\]](#).
- [136] F. Giese, T. Konstandin, and J. van de Vis, Finding sound shells in LISA mock data using likelihood sampling, *JCAP* **11**, 002, [arXiv:2107.06275 \[astro-ph.CO\]](#).
- [137] C. Gowling, M. Hindmarsh, D. C. Hooper, and J. Torrado, Reconstructing physical parameters from template gravitational wave spectra at LISA: first order phase transitions, *JCAP* **04**, 061, [arXiv:2209.13551 \[astro-ph.CO\]](#).